appeared in "Evolution of Structures in Continuous Dissipative Systems", eds. F. Busse and S.C. Müller, Lecture Notes in Physics, Springer Berlin, p.295 (1998)

Electrically Driven Instabilities in Smectic Liquid Crystal Films

Harald Pleiner[1], Ralf Stannarius[2] and Walter Zimmermann[3,4,*]

[1] Max-Planck-Institute for Polymer Research, D-55021 Mainz, Germany

[2] Universität Leipzig, Fakultät der Physik and Geowissenschaften, D-04103 Leipzig, Germany

[3] Institut für Festkörperforschung and FORUM Modellierung, Forschungszentrum Jülich, D-52425 Jülich, Germany

[4] Max-Planck-Institute for Physics of Complex Systems D-01187 Dresden, Germany

Abstract: Various electric field driven instabilities in smectic liquid crystal films are discussed. Some of them resemble instabilities well-known from nematic liquid crystals. These are, for instance, the orientational Frederiks transition and electroconvection. However, the restriction of these two instabilities to two spatial dimensions can only be studied in free-standing smectic films, because free standing nematic liquid crystals are unstable. In addition several instabilities, being distinctive features of smectic liquid crystals are described. These are the undulational instability of the smectic layer structure and film buckling. All these different instability types are coupled in smectic C liquid crystals. For smectic C* liquid crystals films, the polarization Frederiks transition and the subharmonic regime of electroconvection are discussed. Electroconvection experiments with smectic C and C* films are reported that show the surface charge dominated 'vortex mode' and convection of the Carr-Helfrich type, respectively.

1 Introduction

Investigations of instabilities in liquid crystals, especially in nematic liquid crystals have become more and more a common subject of nonlinear science [1, 2, 3, 4, 5]. For a few nematic substances not only qualitative understanding, but also a quantitative agreement between theory and experiment of several instabilities could be achieved during the recent decade. While in nematics the hydrodynamic equations of motion are well established for a long time and the required phenomenological parameters are known to some extent, the situation for smectic liquid crystals is rather different.

Liquid crystals in general are an interesting class of systems to study various aspects of pattern formation. They offer the opportunity to investigate for instance electrically (and magnetically) driven bifurcations, as is well-known for nematic liquid crystals, also in various smectic phases under different symmetry conditions. Additionally in smectic phases new types of

instabilities occur as discussed below.

In the nematic, smectic A (SmA), smectic C (SmC), and smectic C* (SmC*) liquid crystal phases there is an increasing molecular and macroscopic order (fig. 1), which gives rise to additional internal degrees of freedom. In the isotropic phase there is no preferred order of the ellipsoidal organic molecules. In the nematic phase one has an orientational order of the molecules described by a director $\boldsymbol{n}$ and its reorientation can be influenced by external fields. In the smectic A phase (SmA) there is an additional positional order in one spatial direction as indicated in fig. 1a). Layer deformations can be achieved by external fields.

In the smectic C phase the molecules are in addition tilted with respect to the smectic layers, cf. fig. 1a) and the projection of the director $\boldsymbol{n}$ onto the smectic layer plane, the $\boldsymbol{c}$ director, again shows a nematic degree of freedom in the plane of the smectic layers. Hence, the properties in the layer are isomorphic to a two-dimensional nematic, if the layers are assumed to be rigid. The azimuthal position of the tilt direction is not fixed.

In the chiral smectic C* phase there is an in-plane polarization $\boldsymbol{P}$ perpendicular to the (conic helical) director field $\boldsymbol{n}$. How the orientation of $\boldsymbol{n}$ and $\boldsymbol{P}$ change gradually from layer to layer is indicated in fig. 1b) [1]. Accordingly the polarization averages out in the bulk. When the formation of the helix is suppressed by geometrical constraints or can be neglected (i.e. in very thin films), it has similar transport properties as the SmC phase, e.g. an anisotropy of the electric conductivity.

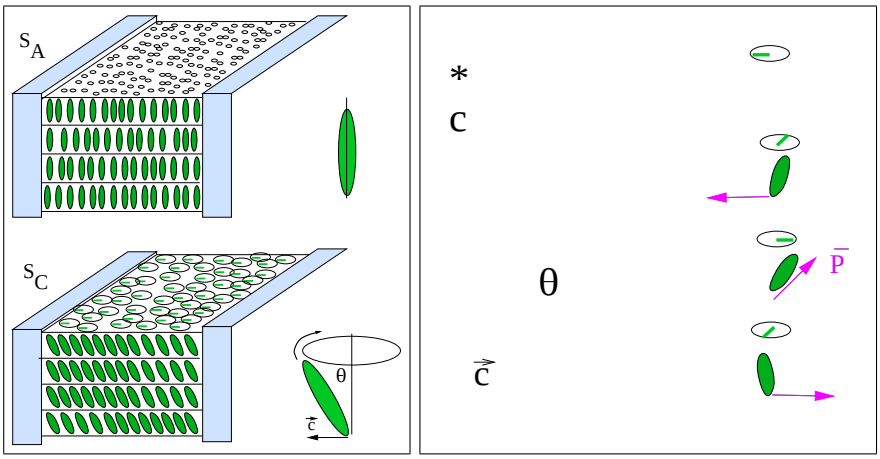

Figure 1: *Sketch of the molecular order in three different smectic liquid crystal phases. The layered structure of the smectic* A *phase* (SmA) *and smectic* C *phase* (SmC) *with the tilted order of molecules on the left and on the right the smectic* C* *phase, where the tilt direction rotates gradually from layer to layer, and where an in-plane polarization is rigidly coupled perpendicularly to the director* $\boldsymbol{n}$.

One consequence of the orientational order in nematic liquid crystals are

anisotropic material properties, such as anisotropic susceptibilities, orientation-elastic moduli and viscosities. According to the anisotropic susceptibilities the director can be switched in external fields. Most famous is the switching of the orientational order in the common liquid crystal displays (see e.g. ref. [6]). It has been observed first in experiments by Frederiks and Tsvetkov already in 1934 [7]. In smectic liquid crystals the orientational order couples to the layer structure which gives rise to additional instabilities such as the Helfrich-Hurault instability (fig. 2), studied up to now in smectic A liquid crystals [1, 8, 9] or general layer deformations [10, 11].

Instead of studying smectic materials in the bulk, freely suspended films are a suitable alternative, which have been discovered about 20 years ago [12, 13]. Like soap films, such smectic films with only a few nanometers or micrometers in thickness can have lateral extensions of several centimeters. The smectic layers are perfectly stacked in the film plane. Figure 1a) visualizes the geometry of freely suspended smectic A and C films. Such stable free standing films allow the design of experiments which are essentially two–dimensional. In contrast, thin nematic or cholesteric films are usually unstable.

Putting free standing smectic films in external fields the preferred orientation can be changed [14], and according to the coupling of the mean orientation of molecules to the orientation of the smectic layers, the smectic layers are also deformed and they ultimately couple also to the shape of the film. Therefore field induced buckling may arise in SmC as discussed in sec. 2.5. In thin films the polarization in the SmC* gives rise to an additional coupling and indeed a novel transition, the so-called polarization Frederiks transition, has been predicted recently [15]. This is described in more detail in sec. 2.6. These different field induced deformations in smectic liquid crystals are usually not independent from each other, but are coupled and give rise to hybrid instabilities as discussed in sec. 2.4.

Electroconvection (EC) has an equally long history in nematic liquid crystals. 30 years after the discovery of electric field effects in thin cells of nematic liquid crystals [7] spatially periodic patterns have been observed by Williams [16] and, at higher applied voltages, the so-called dynamic scattering mode by Kapustin and Larionova [17]. Theoretical understanding of the basic mechanism of electroconvection has been achieved by Carr [18] and Helfrich [19]. The Helfrich theory was later extended by Dubois-Violette et al. [20] to finite frequencies of the AC voltage and to two spatial dimensions in ref. [21]. A number of three-dimensional phenomena have then been observed in experiments as reviewed in refs. [2, 22]. The so-called oblique rolls observed as first instability by Joets and Ribotta [23, 24] triggered an extension of previous theoretical calculations to three dimensions [25, 26], at first linear and then more and more into the nonlinear regime of electroconvection in nematic liquid crystals. The further development in this field during the recent decade has been described in several recent articles [27, 28, 29, 30, 31] and in this volume [32].

Research on electroconvection in smectic liquid crystals is less advanced. The formation of a striped texture induced by electroconvection in smectic A phase ([33, 34, 35] and references therein), in the smectic C phase [36, 37] and in the smectic O phase [38] has been observed. Experiments with rotating electric fields are reported in [39]. In contrast to nematics the possibility of convection depends crucially on the orientation of the layers with respect to the external field. Electric fields perpendicular to the smectic layers hardly induce electroconvection because the layered structure strongly impedes flows perpendicular to the layers. On the other hand electric fields parallel to the smectic layers may induce convective motion essentially restricted to the smectic layers, which enables studies on convection in ideally two-dimensional systems. This has been shown recently for thin SmA films [40, 41], where the convective motion in the thin film can be easily visualized by dust particles, cf. sec. 4.2.

Thin films of smectic C liquid crystals are somewhat similar to two-dimensional nematics (if the layers are fixed) and the convective motion can be analyzed more precisely than in three dimensional nematic layers. Thin films of smectic C^* resemble two-dimensional nematics with an additional polarization perpendicular to the director. For both systems there is a preferred direction in the plane of the film and one may expect that anisotropic transport properties, typical for liquid crystals systems, play a crucial role for electroconvection. Experimental and theoretical results on both systems are described in secs. 3 and 4.3, 4.4.

2 Static Instabilities

In liquid crystals external electric and magnetic fields can induce various static instabilities. In phases with nematic degrees of freedom (e.g. uniaxial nematics) there is an orientational transition of the director, the so-called Frederiks transition [1, 7]. For layered systems (e.g. smectic A) the Helfrich–Hurault effect is possible, where the smectic layers are undulated relatively to each other. In (smectic) films the film can buckle as a whole (buckling instability). In smectic C films all these possibilities are present simultaneously and the instabilities never occur independently, but are always coupled. Nevertheless we discuss them at first independently, and then look step by step how they are coupled.

In this section we discuss *static* instabilities, which would mean, strictly speaking, that no flow (or any other dissipative process) is induced and the stability is governed by a free energy functional. Such purely static instabilities are possible for very clean systems and geometries only, where charges do not have to be considered. Thus, the instabilities discussed below are *static* as an approximation only for dirty systems, insofar the flow and its effect on other degrees of freedom are small and flow is not a relevant part of the instability mechanism itself. The opposite case, where flow is a necessary part of the mechanism, will be discussed in sec. 3.

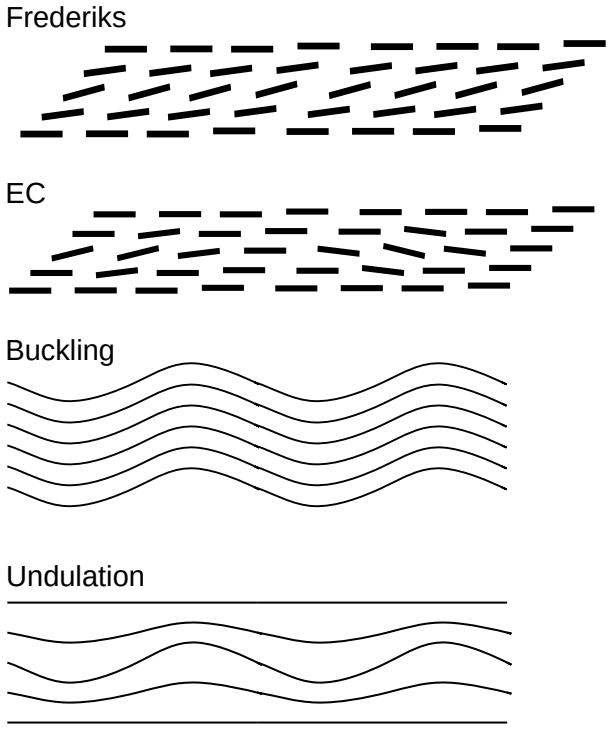

Figure 2: *Sketch of the four instabilities discussed in this article: The orientational transition (Frederiks transition), the buckling instability of smectic layers, the undulation instability (Helfrich–Hurault) in section 2 and the electrohydrodynamic instability (*EC*) in section 3.*

2.1 Theoretical Formulation

In liquid crystals a few continuous symmetries are spontaneously broken and the related hydrodynamic fields are introduced in the following. In the nematic phase the rotational symmetry is spontaneously broken due to the ordering of the molecules. The preferred mean direction is described by the director field $\boldsymbol{n}(\boldsymbol{r},t)$, with $\boldsymbol{n}^2 = 1$ and the constraint that $\boldsymbol{n}$ is equivalent to $-\boldsymbol{n}$ in all equations.

The smectic layering is due to a small periodic modulation of the density along one direction (the layer normal). This denotes a spontaneously broken translational symmetry in one direction. Within the layers a smectic A phase is isotropic and liquid. The layering is described by a scalar 'phase' variable $\phi(\mathbf{r},t)$, which can be thought of numbering all layers (it is integer in the middle of each layer). The layer normal is then defined by [42]

$$\boldsymbol{k} = \frac{\boldsymbol{\nabla}\phi}{|\boldsymbol{\nabla}\phi|} \qquad \leftrightarrow \qquad \boldsymbol{k}\cdot\delta\boldsymbol{k} = 0\,. \tag{1}$$

Generally the area $\phi(\boldsymbol{r},t) = const.$ can have any shape, although in the ther-

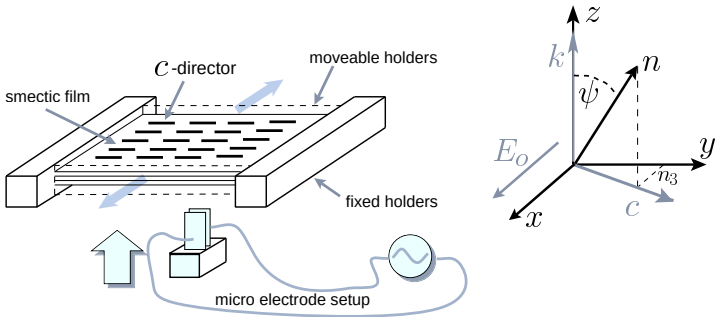

Figure 3: *Sketch of an experimental arrangement of a* SmC *film. The notation is as introduced in the text.*

modynamically stable case these are flat layers. Without restriction of generality one can choose

$$\phi_{\,\mathrm{flat}}(\boldsymbol{r}) \;=\; z \;, \tag{2}$$

while deformations of this flat ground state are described by a displacement vector $\boldsymbol{u}(\boldsymbol{r},t)$, which is the appropriate variable according to the broken translational symmetry,

$$\phi \;=\; z - \boldsymbol{u}\cdot\boldsymbol{k} \;. \tag{3}$$

However, only displacements perpendicular to the layers are relevant, since the layers themselves are fluid. Thus

$$\boldsymbol{k}\times\boldsymbol{u} = 0 \quad \leftrightarrow \quad \delta\boldsymbol{k}\times\boldsymbol{u} + \boldsymbol{k}\times\delta\boldsymbol{u} = 0 \quad . \tag{4}$$

If the deformations of the flat layers are small (and we will assume that case in the following), all expressions can be expanded into gradients of the relevant variable $u = \boldsymbol{u}\cdot\hat{\boldsymbol{e}}_z$ and we have

$$\boldsymbol{\nabla}\phi = \hat{\boldsymbol{e}}_z - \boldsymbol{\nabla}u \;, \tag{5}$$

$$|\boldsymbol{\nabla}\phi| - 1 = \sqrt{1 - 2\nabla_z u + (\boldsymbol{\nabla}u)^2} - 1 \approx -\nabla_z u + \frac{1}{2}(\boldsymbol{\nabla}_\perp u)^2 \;, \tag{6}$$

where $\boldsymbol{\nabla}_\perp = (\nabla_x, \nabla_y, 0)$ denotes gradients perpendicular to the (undistorted) layer normal.

In the smectic C phase (SmC) the director is tilted with respect to the layer normal

$$\cos\theta = \boldsymbol{k}\cdot\boldsymbol{n} = \text{const.} \quad \leftrightarrow \quad \boldsymbol{k}\cdot\delta\boldsymbol{n} - \boldsymbol{n}\cdot\delta\boldsymbol{k} = 0. \tag{7}$$

The (normalized) projection of $\boldsymbol{n}$ onto the layers is called the $\boldsymbol{c}$ director. Thereby rotational symmetry within the layers is spontaneously broken and SmC is biaxial. Thus SmC combines both, a smectic degree of freedom (u) and one that is nematic-like [43],

$$n_3 = \frac{\boldsymbol{n}\times\boldsymbol{k}}{|\boldsymbol{n}\times\boldsymbol{k}|}\cdot\delta\boldsymbol{n} \;, \tag{8}$$

and which describes rotations of the director about the layer normal (thus conserving the tilt angle θ). In fig. 3 the geometry is illustrated. The external electric field is applied perpendicular to both, the undistorted layer normal and the director.

Static distortions of the SmC structure subject to an external field are given by the free energy density [1, 44]

$$\begin{aligned} 2\tilde{\varepsilon} &= -\epsilon_1 (\boldsymbol{E}\cdot\boldsymbol{n})^2 - \epsilon_2 (\boldsymbol{E}\cdot\boldsymbol{k})^2 - \epsilon_3 \boldsymbol{E}^2 - 2\,\epsilon_4 (\boldsymbol{E}\cdot\boldsymbol{n})(\boldsymbol{E}\cdot\boldsymbol{k}) \\ &\quad + B\left(\nabla_z u - \frac{1}{2}(\boldsymbol{\nabla}_\perp u)^2\right)^2 + \mathcal{T}_{ijkl}\,(\nabla_i\nabla_j u)(\nabla_l\nabla_k u) \\ &\quad + \mathcal{F}_{ij}\,(\nabla_i n_3)(\nabla_j n_3) + 2\,\mathcal{C}_{ijk}(\nabla_i n_3)(\nabla_j\nabla_k u)\,, \end{aligned} \tag{9}$$

where the first line describes the dielectric coupling of the field to both, the layer normal and the director. The second line gives the elastic distortion energy due to layer distortions, while the third one contains the orientational-elastic energy due to director distortions and the static couplings between director and layer distortions, respectively. The materials tensors $\mathcal{F}_{ij}$, $\mathcal{T}_{ijkl}$, $\mathcal{C}_{ijk}$ contain 4 (F_{11}, F_{22}, F_{33}, F_{13}), 6 (C_1,...,C_6), and 9 (T_1,...,T_9) coefficients, respectively, according to the monoclinic symmetry of SmC [43].

The dynamics of such distortions is described by balance equations for the director as well as for the layers. They are of the scalar form

$$\frac{d}{dt}\,u + X \;=\; \frac{\partial}{\partial t}\,u + \boldsymbol{v}\cdot\boldsymbol{\nabla}u + X \;=\; 0\;, \tag{10}$$

$$\frac{d}{dt}\,n_3 + Y \;=\; \frac{\partial}{\partial t}\,n_3 + \boldsymbol{v}\cdot\boldsymbol{\nabla}n_3 + Y \;=\; 0\;, \tag{11}$$

with $\boldsymbol{v}$ the velocity field. The quasi-currents X and Y contain the dynamic couplings to the additional hydrodynamic degrees of freedom, like mass density, momentum density and energy density [43, 45, 46]. For static distortions the explicit form of X and Y is not needed and we will discuss them in sec. 3 only.

2.2 Frederiks Transition

The most famous transition in liquid crystals is the Frederiks transition [1, 7], which is an orientational transition of the director driven by an external field via the anisotropies in the dielectric (and diamagnetic) susceptibilities. This orientational transition is crucial for the functioning of the modern liquid crystal displays [6].

In smectic C liquid crystals director rotations are described by n_3. Neglecting all (static and dynamic) cross-couplings to other variables the free energy (9) has an extremum if

$$\left(F_{11}\,\frac{\partial^2}{\partial y^2} + F_{22}\,\frac{\partial^2}{\partial x^2} + F_{33}\,\frac{\partial^2}{\partial z^2} + 2\,F_{13}\,\frac{\partial^2}{\partial z\,\partial y} + \epsilon_1 E_o(t)^2\right) n_3 = 0\;. \tag{12}$$

The F_{ij}'s are generalized Frank constants [44] and ϵ_1 is one of the susceptibility anisotropies. The symmetry of eq. (12), $x \to -x$ and $(y,z) \to (-y,-z)$, reflects the reduced symmetry of the SmC phase. Stability of the ground state ($n_3 = 0$) is probed with respect to periodic distortions

$$n_3 = \left[n_{3,c} \cos(k_y \pi y) \, \cos\left(\frac{z\pi}{d_z}\right) + n_{3,s} \sin(k_y \pi y) \, \sin\left(\frac{z\pi}{d_z}\right) \right] \cos(k_x \pi x) \; . \quad (13)$$

This simple ansatz does not fix n_3 at the top and bottom of the film ($z = \pm d_z/2$); a z-dependence is assumed in order to describe the 3-dimensionality of the system (layer undulations are taken into account more realistically below); the y-direction is assumed to be infinite, so k_y is continuous and has to be determined by minimizing the threshold; since the electrodes are assumed to be rigid boundaries for the director, the lowest possible value for k_x is $k_x = 1$ in dimensionless units. The threshold condition follows from inserting the ansatz (13) into eq. (12) and reads [47]

$$E^2_{fred\ 1,2} = \left(F_{11} k_y^2 + F_{22} k_x^2 + F_{33} \frac{1}{d_z^2} \pm 2 F_{13} k_y \frac{1}{d_z} \right) \frac{\pi^2}{\epsilon_1} \, . \quad (14)$$

The critical wavelength is given by

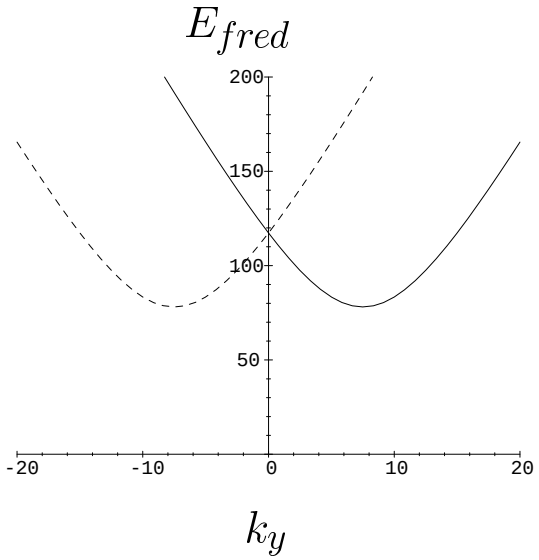

Figure 4: *Frederiks threshold in thin films with ($F_{ii} = 1$, $F_{13} = 0.75$, $k_x = 1$, $d_z = 0.1$), cf. eq. (14)* [47].

$$| \, k_{yc} \, | \quad = \quad \frac{| \, F_{13} \, |}{F_{11}} \, \frac{1}{d_z} \quad (15)$$

In fig. 4 the threshold field strength is plotted against the wavelength k_y. The minimum at non-zero wavelength indicates that the variation of the director

field depends on all three coordinates in contrast to nematics, where F_{13} is zero and the director field varies only along the x-direction. Although the simplified analytical treatment of this section cannot lead to quantitatively correct results, the qualitative result of 3-dimensional patterns survives a more complete treatment taking into account layer undulations, additionally.

2.3 Undulational Instability

We will now come to the opposite special case, where the director is kept fixed but the layers can move. In this subsection we assume that the smectic film stays flat on average, i.e. the layers undulate such that either the upper and lower layer or the middle one is fixed. An overall buckling of the film is considered in sec. 2.5.

An external field tends to reorient the layer normal according to the dielectric anisotropy. Since the layers cannot rotate homogeneously, they undulate, thus creating regions, where the layer normal is rotated. This happens if the electric field is strong enough to overcome the elastic and bending-elastic energy involved. Neglecting dynamic effects the state is determined by minimizing the free energy (9), while keeping only contributions involving the layer distortion u

$$\bar{\epsilon}E_o^2(t)\frac{\partial^2 u}{\partial x^2} - B\frac{\partial^2 u}{\partial z^2} + 6\,T_4\frac{\partial^4 u}{\partial x^2\partial z^2} + T_3\frac{\partial^4 u}{\partial x^4} + T_1\frac{\partial^4 u}{\partial z^4} + T_2\frac{\partial^4 u}{\partial y^4} + 2\,T_5\frac{\partial^4 u}{\partial y^2\,\partial x^2}$$
$$+12\,T_7\frac{\partial^4 u}{\partial z\,\partial y\,\partial x^2} + 4\,T_9\frac{\partial^4 u}{\partial z\,\partial y^3} + 2\,T_6\frac{\partial^4 u}{\partial z^2\,\partial y^2} + 4\,T_8\frac{\partial^4 u}{\partial z^3\,\partial y} = 0. \qquad (16)$$

with $\bar{\epsilon} = \epsilon_2 + 2\,\epsilon_4\cos\psi + \epsilon_1\cos^2\psi$. For a simplified analytic discussion we choose an ansatz for u

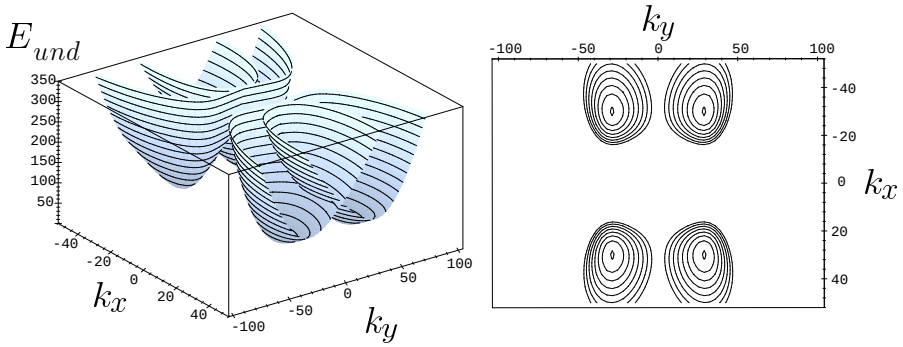

Figure 5: *Undulational threshold (18) for thin films* $d_z = 0.1$ *with* $T_i = 1$. *The undulation is periodic also in y-direction* [47].

$$u = \left[u_s\,\sin(k_y\pi y)\,\sin\left(z\frac{\pi}{d_z}\right) + u_c\,\cos(k_y\pi y)\,\cos\left(z\frac{\pi}{d_z}\right)\right]\,\cos(k_x\pi x), \qquad (17)$$

that allows 3-dimensional patterns, is compatible with the smectic C symmetry, and denotes no-slip conditions for the layers at the electrodes, but cannot accommodate fixed boundary conditions for the first and last layers ($z = \pm d_z/2$). For more realistic boundary conditions numerical methods are necessary. This immediately leads to the threshold conditions

$$\begin{aligned}\bar{\epsilon}\, d_z^2\, k_x^2 \pi^{-2} E_{und\,1,2}^2 = {} & B\pi^{-2} + T_1\, d_z^{-2} + T_2\, k_y^4\, d_z^2 + 6\, T_4\, k_x^2 + T_3\, k_x^4\, d_z^2 \\ & + 2\, T_6\, k_y^2 + 2\, T_5\, k_y^2\, k_x^2\, d_z^2 \pm 4 k_y d_z (3\, T_7\, k_x^2 + T_8 d_z^{-2} + T_9\, k_y^2)\end{aligned} \tag{18}$$

for the two eigenvalues $\{u_s, u_c\} = \{1, \pm 1\}$. The true threshold is the minimum of E_{und}^2 with respect to k_x and k_y (strictly speaking, $k_x = n + 1/2$ with $n \geq 1$ is discrete). Analytically this leads to rather involved equations so we present the graphical solution in fig. 5, where one can clearly see that the lowest threshold value is obtained at a finite critical wave vector k_y indicating truly 3-dimensional patterns in contrast to the Helfrich-Hurault instability in smectics A.

For thicker films, however, the critical k_y decreases with the film thickness and finally an almost 2-dimensional pattern is found (fig. 6). In that case the

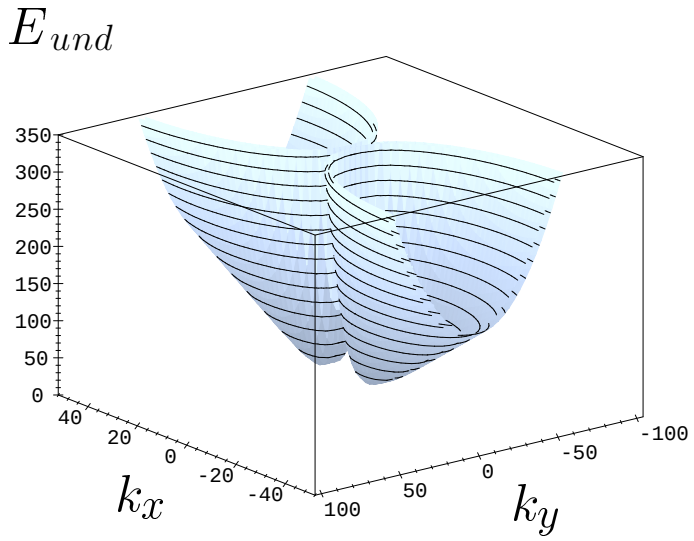

Figure 6: *Undulational threshold (18) for thick films $d_z = 1$. The wave vector k_y tends to zero, while k_x remains finite, but small. ($T_i = 1$)* [47].

threshold condition (18) can be simplified into

$$\bar{\epsilon}\, d_z^2\, k_x^2 \pi^{-2} E_{und\,1,2}^2 = B\pi^{-2} + T_1\, d_z^{-2} + 6\, T_4\, k_x^2 + T_3\, k_x^4\, d_z^2 \tag{19}$$

Minimization of this expression with respect to k_x leads to the critical value

$$k_{xc}^2 = \frac{1}{\pi d_z^2} \sqrt{\frac{T_1 \pi^2 + B d_z^2}{T_3}}\,. \tag{20}$$

The film thickness dependence of the threshold field (fig. 7) is slightly different from the $E^2 \propto 1/d_z$ behavior.

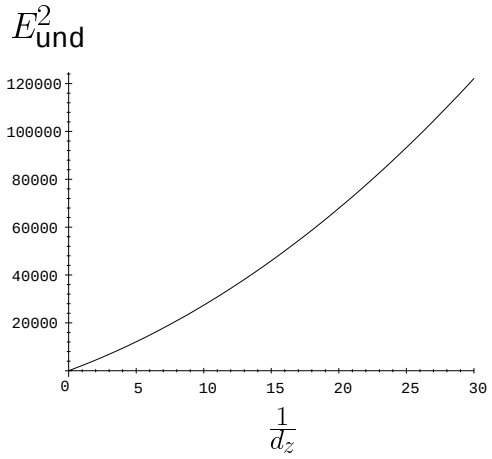

Figure 7: *Dependence of the undulational threshold on the (reciprocal) film thickness for thick films. ($T_i = 1$; $B = 10^5$, $\epsilon_1 = -0.072$, $\epsilon_2 = 1$, $\epsilon_4 = 0$)* [47].

2.4 Interaction between Instabilities

In the last two subsections we have discussed director and layer instabilities separately by deliberately neglecting coupling terms. Here we will give an example how the coupling terms can affect the instabilities. We could combine the two types of ansatz (13) and (17) and look for combined layer and director distortions. However, this is still too complicated for the analytical treatment, since it leads to 4x4 matrix problem. Thus, we choose the even more simplified mode ansatz

$$\begin{aligned} n_3 &= n_o \cos(k_x \pi x) \cos(k_y \pi y) \cos(z \frac{\pi}{d_z}) \,, \\ u &= u_o \sin(k_x \pi x) \cos(k_y \pi y) \cos(z \frac{\pi}{d_z}) \,, \end{aligned} \tag{21}$$

which, however, is only sufficient, if we assume in addition

$$C_1 = C_4 = T_7 = T_8 = T_9 = F_{13} = 0 \,. \tag{22}$$

The conditions (22) mean that we have eliminated all contributions responsible for the 3-dimensionality of the resulting instability pattern. Indeed $k_y = 0$ is found for the critical wave vector in y-direction. Of course, a more sophisticated treatment would regain 3-dimensional structures.

The threshold condition is obtained by minimizing the free energy using eq. (21) and can be written in the form $\det(L_{ij}) = 0$, where the elements of

the 2x2 matrix are,

$$
\begin{aligned}
L_{11} &= \pi^2\,[k_y^2 F_{11} + k_x^2 F_{22} + d_z^{-2} F_{33}] - \epsilon_1 E_o(t)^2, \qquad (23)\\
L_{12} = L_{21} &= \pi k_x[\epsilon_1\,\cos\psi\,E_o(t)^2 \,+\, \epsilon_4\,E_o(t)^2\\
&\quad +\pi^2 k_y^2 C_2 + \pi^2 d_z^{-2} C_3 + 2\,\pi^2 d_z^{-2} C_5 + k_x^2 \pi^2 C_6],\\
L_{22} &= \pi^4\,[k_y^4\,T_2 + 6\,k_x^2 d_z^{-2}\,T_4 + 2\,k_y^2 d_z^{-2}\,T_6 + k_x^4\,T_3 + d_z^{-4}\,T_1\\
&\quad +2\,k_x^2 k_y^2\,T_5] + \pi^2\,[d_z^{-2} B - \bar{\epsilon}\,k_x^2 E_o(t)^2].
\end{aligned}
$$

The coupling of the layer and director instabilities is provided by the (remaining) coupling coefficients C_i as well as by the dielectric anisotropy $\epsilon_{1,4}$. We will not write down the analytical threshold condition, but give the graphical representation of the neutral curve for different film thicknesses.

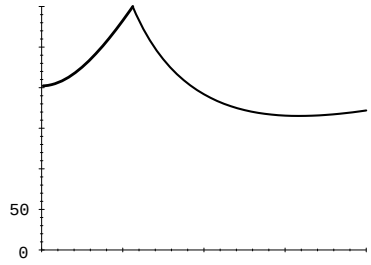

Figure 8: *Neutral curves of the combined layer and director instabilities for different film thicknesses (choosing* 0.9, 3, 1 *for the non-zero* C_i, F_{ii}, *and* T_i *parameters, respectively)* [47].

In both cases two distinct instabilities are visible, the Frederiks-like one at zero wave vector and the undulation-like one at finite k_x. However, the unstable mode always contains both, layer and director distortions. Nevertheless the qualitative nature (the basic mechanism) of the instabilities is still preserved. The reason for this "weak" coupling is the large difference of critical wave vectors of the underlying decoupled instabilities. Note that the minimum of the threshold switches from one instability to the other by changing the film thickness.

In order to get a more realistic treatment one has to take into account, firstly, all variables, e.g. the electrical potential ϕ^{el}, defined by $\boldsymbol{E} = \boldsymbol{E}_0 - \boldsymbol{\nabla}\phi^{el}$. Secondly, the full dynamics has to be considered and finally more spatial modes (which obey realistic boundary conditions) have to be included in order to get a better characterization of the patterns. In the case of external AC fields (with frequency ω) also temporal modes are needed. Then only a numerical treatment is possible. The basic procedure is described in the EC section below.

For the 3-dimensional smectic C case and for a special set of parameters, the following neutral stability curves are obtained (fig. 9). For large Frank-like

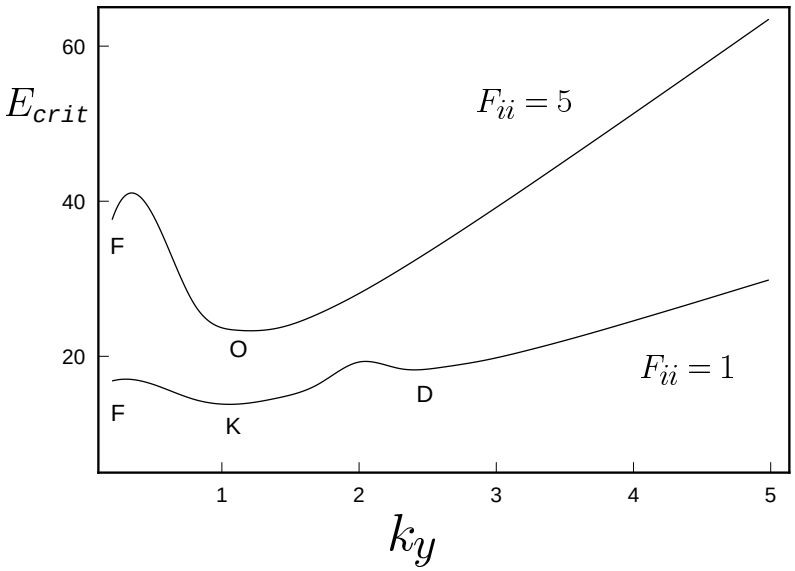

Figure 9: *Numerical neutral curves for different values of the Frank-like constants ($F_{ii} = 1, 5$) and positive dielectric anisotropy ($\epsilon_1 = +0.0724$, $d_z = 1$, $\omega = 100$, free boundary conditions)* [47].

constants there are two minima (instabilities), which again can be characterized as Frederiks- (F) and undulation-like (O). The corresponding eigenvectors are visualized in figs. 10 and 11, respectively. There, the contributions of the variables (including the velocity components vx= v_x, vz= v_z and the electric potential Phi= ϕ^{el}, which have been neglected before) to the eigenvector are shown in a grey scale (white = zero), either in the x/y plane or the temporal evolution along a line $y = const.$ (t/x plane). Across the film suitable mean values have been taken, i.e. $u(x, y) = (\int \mid u(x, y, z) \mid^2 dz)^{1/2}$.

For small Frank-like constants ($F_{ii} = 1$) the undulation-type instability is gone and two new ones (K and D) occur. They are related to electroconvection.

2.5 Buckling Instability

In the previous subsections we have assumed that the film as a whole stays flat when subjected to an external field and only the layers inside the film are undulated and compressed or dilated. Now we will consider the opposite case that the film as a whole buckles and all layers inside follow homogeneously (cf. fig. 2). Of course, one could think of a mixed case, where buckling and undulations occur simultaneously, but it is hard to see, how the system could gain from that.

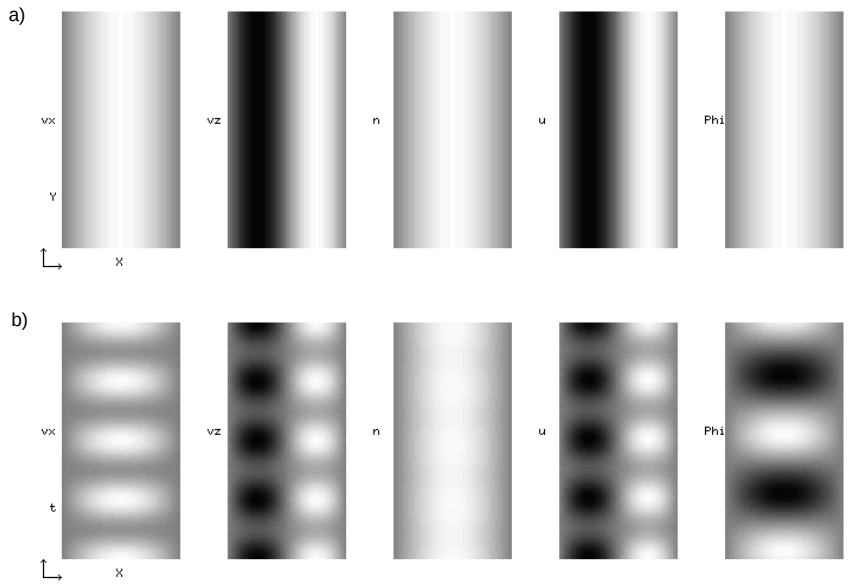

Figure 10: *Frederiks-like instability with layer undulations (and flow),* $k_y = 0$, *corresponding to minimum* F *in fig. 9 (*$F_{ii} = 5$*)* [47].

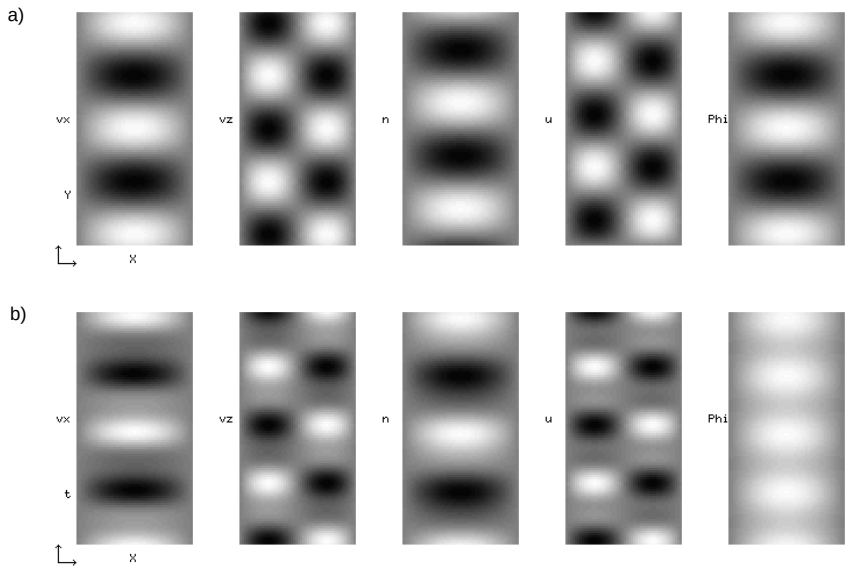

Figure 11: *Undulation-like instability with director reorientation (and flow),* $k_y \neq 0$, *corresponding to minimum* O *in fig. 9 (*$F_{ii} = 5$*)* [47].

For the homogeneous buckling there is no z-dependence and the system can be treated two-dimensionally. Because of that the cost in elastic energy seem to be smaller for buckling than for undulations and one could infer that the threshold field for layer buckling should always be lower than that for undulations. However, there is another important point to be considered with buckling. If the film is and stays flat, the electrostatics is trivial. The electric field is homogeneous (like in a plate capacitor) inside and outside the film (we always assume infinitely large electrodes). However, when the film buckles this is no longer true and the electric potential will be distorted by the curved boundary between the (dielectric) film and the air above and below. Thus there is additional dielectric energy involved due to the buckling of the film, which can drive the buckling threshold beyond that for undulations.

The proper treatment for the buckling instability would be to solve the hydrodynamic equations together with the electric boundary problem. Since the boundaries are moving according to the solution of the whole problem, this is a very intricate problem. In order to get some insight analytically, we will simplify it by assuming that the influence of the curved boundaries can be treated electrostatically and in a coarse grained fashion. First we notice that the electrical potential ϕ^{ind}, induced by the film buckling, is proportional to $\nabla_x u$. Since ϕ^{ind} has to vanish at the electrodes and since it is the solution of Laplace's equation outside the film (and a somewhat more complicated equation inside, because of the dielectric anisotropy) the appropriate ansatz for film buckling is

$$u = u_o \cos^2(k_x \pi x)\, \cos(k_y \pi y)\,. \tag{24}$$

Neglecting all cross-couplings to other variables and taking into account only the elastic and dielectric anisotropy energy (9), but neglecting for the moment the buckling induced electric energy, the neutral curve for buckling would be [47]

$$4\,\bar{\epsilon}\,k_x^2 \pi^{-2}\, E^2_{buck}(noinduced) = 3\,k_y^4\,T_2 + 16\,k_x^4\,T_3 + 8\,k_x^2 k_y^2\,T_5 \tag{25}$$

It is easy to notice that the critical wave vector k_y is zero, while k_x cannot be smaller than 1. This describes a 1-dimensional pattern above the threshold (the neglected cross-couplings would recover a finite k_y, i.e. a 2-dimensional pattern)

$$E^2_{buck}(k_x = 1; k_y = 0; noinduced) \;=\; 4\,\frac{T_3\,\pi^2}{\epsilon_z - \epsilon_x}\,, \tag{26}$$

with the abbreviations

$$\epsilon_x = \epsilon_3\,, \qquad\qquad \epsilon_z = \bar{\epsilon} + \epsilon_3 = \epsilon_2 + \epsilon_3 + 2\,\epsilon_4 \cos\psi + \epsilon_1 \cos^2\psi\;. \tag{27}$$

However, we still have missed the extra dielectric energy due to electric potential induced by the curved boundaries. Taking a buckled film described by a fixed displacement (24) with $k_y = 0$ the electrostatic boundary problem can be solved by standard means. In the limit of thin films and averaging over space the electric energy density within the film at a given buckling amplitude

u_0 is found to be

$$\tilde{\varepsilon}'_{buck-el} \;=\; -\frac{1}{2}\,\epsilon_x E_o^2 + \frac{\pi^2}{4}\,E_o^2\,u_o^2\,(\epsilon_x - \epsilon'_z)\;, \tag{28}$$

with

$$\epsilon'_z \;=\; \epsilon_z \;+\; \frac{1}{\pi d_z\sqrt{\epsilon_x\epsilon_z}}\Big[\frac{1}{2}\,\sinh\left(2\pi\sqrt{\frac{\epsilon_x}{\epsilon_z}}\,d_z\right)(\epsilon_z-1)^2 \tag{29}$$
$$+2\sinh\left(\pi\sqrt{\frac{\epsilon_x}{\epsilon_z}}\,d_z\right)(\epsilon_z-1)(1-\frac{\epsilon_z}{\epsilon_x})\epsilon_x\Big]\;.$$

This electric energy density (28) has exactly the same form as the dielec-

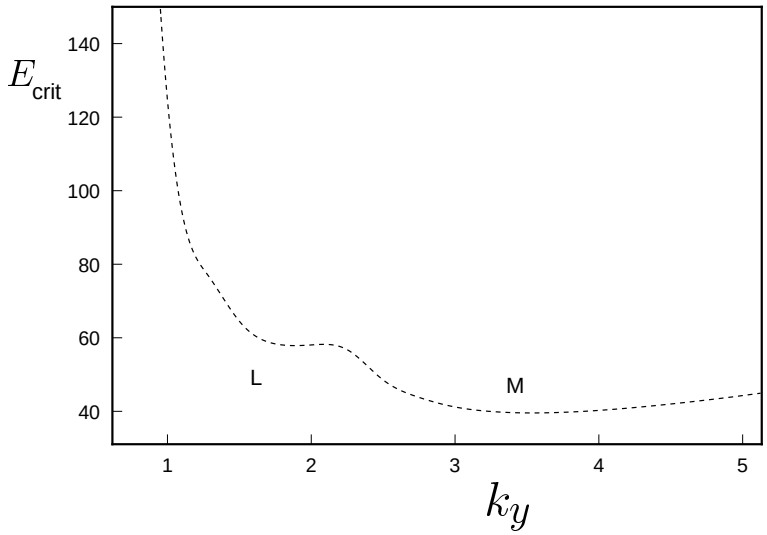

Figure 12: *Neutral instability curve involving film buckling, director reorientation and EC (flow) for negative dielectric anisotropy. The patterns are 2-dimensional and minimum* M *corresponds to an EC-like instability, while minimum* L *is qualitatively new* [47].

tric anisotropy energy density (i.e. the electric energy density without the buckling-induced part) except that there ϵ_z occurs instead of ϵ'_z. Vice versa this means that in this approximation the buckling-induced electric energy can be accounted for by replacing ϵ_z by ϵ'_z in the free energy expression (9). Then the buckling threshold is obtained from (26) as

$$E^2_{buck}(k_x = 1; k_y = 0) \;=\; 4\,\frac{T_3\;\pi^2}{\epsilon'_z - \epsilon_x}\;. \tag{30}$$

In the numerical stability analysis one can take into account all cross-couplings, the dynamics, more spatial (and temporal) modes for a given parameter set, but still treats the buckling-induced electric energy as described above.

It is found that buckling couples "strongly" to the other types of instability in the sense that not only all basic instability types occur in mixed form, but that new instabilities arise that are not present in any of the limiting cases. E.g. the minimum L in fig. 12 (which can be the absolute minimum for a different parameter set) is neither present in the pure buckling, nor in the Frederiks, nor in the pure EC case and is, thus, qualitatively different from those. A more detailed discussion of the numerical stability analysis of smectic layers under external electric field will be given elsewhere.

2.6 Polarization Frederiks Transition

In the previous sections we have discussed exclusively achiral smectic C films. We now switch to the chiral smectic C* phase, where not only is the director conic helical but also there is an in-plane polarization always parallel to the director. Due to the helical nature of this polarization the electrostatic boundary problem at the electrodes is non-trivial even in the ground state. We therefore assume the helical pitch much larger than the film thickness, which allows us to neglect the helix. The problem is then homogeneous across the film. Since we want to concentrate on the influence of the polarization on the Frederiks transition, we also assume the layers to be fixed. The problem is then strictly 2-dimensional. The advantage is that within this approximation not only the linear stability problem is feasible, but also the complete nonlinear stability problem can be obtained.

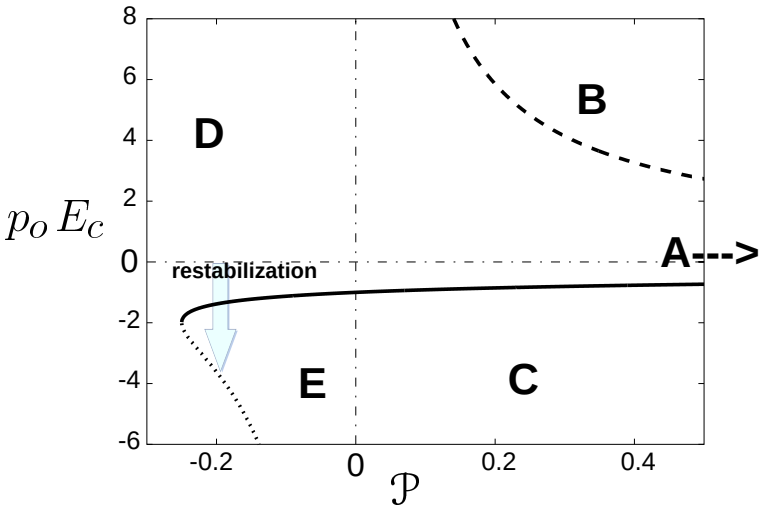

Figure 13: *The threshold field E_c of the generalized Frederiks transition as function of the material parameter combination $\mathcal{P} = \epsilon_1/p_o^2$. The region* E *allows for a possible restabilization* [15].

In the achiral case the sign of the dielectric anisotropy ϵ_1 governs the stability. In the geometry chosen ($\boldsymbol{n} \perp \boldsymbol{E}$) positive (negative) ϵ_1 characterizes a

dielectric unstable (stable) situation. In the chiral case the polarization stabilizes (destabilizes) the structure according to the ferroelectric coupling, if it is parallel (antiparallel) to the external field. Since the in-plane polarization is rigidly connected to the director both (in)stability mechanisms work together, either constructively or destructively. Most interesting is the case, where the situation is dielectrically stable but ferroelectrically unstable. Since the ferroelectric coupling is linear in the external field, it will win for small fields, while the dielectric stabilization gains at higher field strengths. Thus one can expect – with increasing field – first an instability (the combined structure of director and polarization rotates) to occur, while then either a restabilization to the ground state occurs, or the structure rotates further so that the director and the polarization have turned by π (except at the boundaries), which is a genuinely stable situation. The detailed theory [15, 48] shows on what parameters the different scenarios depend.

First we have to add the ferroelectric energy to eq. 9,

$$\tilde{\varepsilon}_p = \tilde{\varepsilon} - P_i E_i \ . \tag{31}$$

Since we can neglect flow, we are left with two variables, the induced electric potential ϕ^{el}, defined by $\boldsymbol{E} = \boldsymbol{E_0} - \boldsymbol{\nabla}\phi^{el}$ and the rotation of the in-plane director $\boldsymbol{c}$. With the ansatz

$$\boldsymbol{c} = (\sin\theta,\ \cos\theta,\ 0)\,, \qquad\qquad \boldsymbol{P} = p_o\,(\cos\theta,\ -\sin\theta,\ 0)\,, \tag{32}$$

one gets two partial differential equations for θ and ϕ^{el} at the threshold postulating the electric current as well as the torque on the director (and on the polarization) to vanish [49]

$$\begin{aligned} &\left(F_{11}\sin^2\theta\ +\ F_{22}\cos^2\theta\right)\ \nabla_x^2\theta - p_0\ \sin\theta\,(E_o - \nabla_x\phi^{el}) \\ &+\left(\,(F_{11}-F_{22})(\nabla_x\theta)^2 + \epsilon_1(E_o-\nabla_x\phi^{el})^2\,\right)\sin\theta\ \cos\theta = 0\,, \end{aligned} \tag{33}$$

$$\begin{aligned} &\sigma_{xx}\left(2\cos\theta\ \sin\theta\,(\nabla_x\theta)(E_o-\nabla_x\phi^{el}) - \cos^2\theta\,(\nabla_x^2\phi^{el})\right) \\ &+\sigma_{yy}\left(2\cos\theta\ \sin\theta\,(\nabla_x\theta)(E_o-\nabla_x\phi^{el}) - \sin^2\theta\,(\nabla_x^2\phi^{el})\right) = 0\,. \end{aligned} \tag{34}$$

where σ_{xx} and σ_{yy} are the in-plane electric conductivities. The external field is chosen to be static, in order to prevent the ferroelectric effect to be averaged out. Planar boundary conditions are chosen such that the ground state is given by $\theta = 0 = \phi^{el}$.

In order to get the linear stability threshold it is enough to consider θ with the ansatz $\theta(x) = A_o\cos\pi x$. Equation (33) immediately leads to [15]

$$p_o E_{c1,2} = \frac{1}{2\mathcal{P}}\left(1 \pm \sqrt{1+4\mathcal{P}F_{22}}\right)\,, \qquad \text{with} \qquad \mathcal{P} \equiv \frac{\epsilon_1}{p_o^2}\,, \tag{35}$$

which is visualized in fig. 13. Case A corresponds to the well-known achiral case ($\mathcal{P}\to\infty$, or $\epsilon_1\to\infty$, $p_0\to 0$), with the two thresholds $E_c = \pm\sqrt{F_{22}/\epsilon_1}$.

In region B (C) the ferroelectric torque stabilizes (destabilizes) and the Frederiks transition threshold is increased (decreased) compared to the achiral case. In region D both effects are stabilizing and no instability results. Region E (ferroelectrically unstable, dielectrically stable) is the most interesting one showing a possible restabilization. An instability is possible for $p_0 > \sqrt{-4\epsilon_1 F_{22}}$ only. For that region we have performed a weakly nonlinear analysis resulting in an amplitude equation of the form

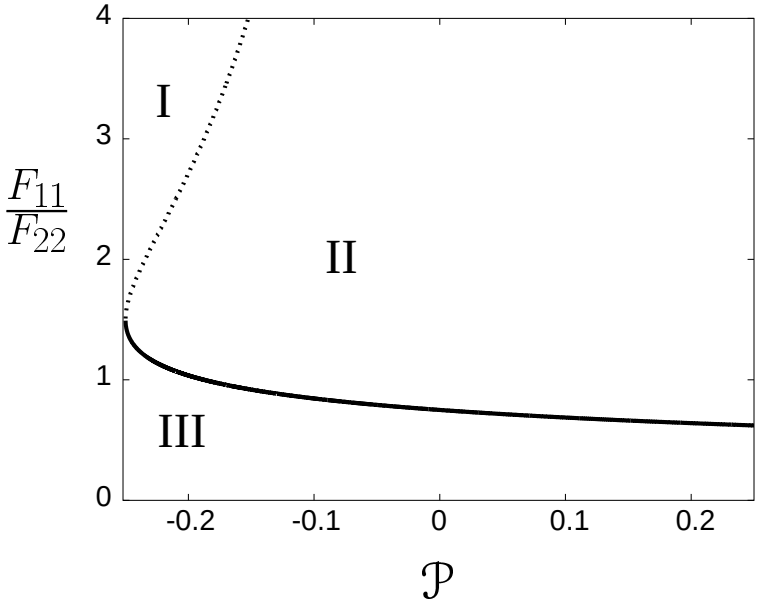

Figure 14: *The zeros of $g_{1,2}$ denoting the boundaries, where the instabilities change their nature (see text)* [15].

$$\tau_o \partial_t A = \left(\eta_{1,2} - g_{1,2} A^2\right) A\,, \tag{36}$$

with

$$g_{1,2} = \frac{3}{8}\,\frac{1 + \frac{8}{3} F_{11}\mathcal{P} \pm \sqrt{1 + 4\mathcal{P}F_{22}}}{1 + 4\mathcal{P}F_{22} \pm \sqrt{1 + 4\mathcal{P}F_{22}}}\,, \quad \tau_o = \frac{2\mathcal{P}}{1 + 4\mathcal{P}F_{22} \pm \sqrt{1 + 4\mathcal{P}F_{22}}}\,. \tag{37}$$

where $\eta_{12} = (E_o - E_{c1,2})/E_{c1,2}$ are the reduced relative threshold fields for the Frederiks instability and the restabilization, respectively. The upper (lower) sign refers to the stabilization (restabilization) curve. The nature of the bifurcation changes (continuous / discontinuous, forward / backward), where the cubic coefficient $g_{1,2}$ changes sign. The zeros of $g_{1,2}$ are shown in fig. 14 as function of the relevant parameters. In region I both instabilities are continuous, in region II the restabilization has become discontinuous, while in region III both instabilities are discontinuous.

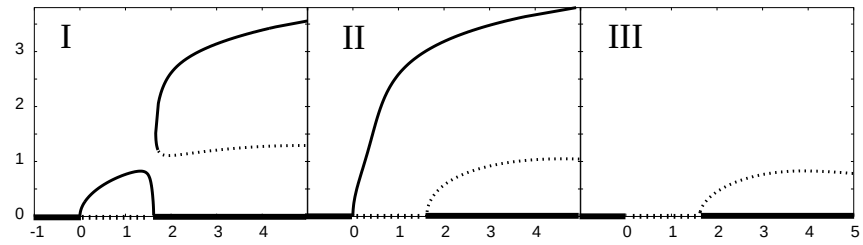

Figure 15: *The amplitude B as function of the reduced external field $\eta_1 = (E_0 - E_{c1})/E_{c1}$ for different values of $F_{11}/F_{22} = 2.9, 1.5, 0.5$. Dotted lines show unstable states* [15]. *The ground state is stable again for $\eta_1 > \eta_r = (E_{c2} - E_{c1})/E_{c1}$.*

The weakly nonlinear analysis is valid only near the threshold, where the amplitudes are still small. For large amplitudes, i.e. in order to investigate the restabilization behavior, we have performed a numerical integration of eqs. 33 and 34. With fixed boundary condition $\phi^{el}(x = \pm 1/2) = \theta\,(x = \pm 1/2) = 0$ a standard shooting procedure is used. The states are characterized by an amplitude B

$$B = \frac{1}{2} \int_{-1/2}^{1/2} \theta(x)\, dx \ , \tag{38}$$

which reduces to the amplitude A_0 introduced in the linear case. In the ground state and the restabilized state $B = 0$. For special values of F_{11}/F_{22} the three regimes I, II, and III are regained (fig. 15). As one can see from this figure, the large amplitude behavior (restabilization or not) is very closely related to the small amplitude behavior (forward or backward bifurcation). In region I, where both bifurcations (at $\eta_1 = 0$ and $\eta_1 = \eta_r$) are continuous, the restabilized ground state above η_r is actually reached. In regimes II and III, where at least one bifurcation is discontinuous, the restabilized ground state

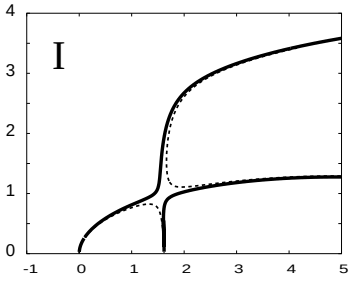

Figure 16: *Example of regime* I *(restabilization bifurcation is continuous), where the restabilized ground state is not reached ($F_{11}/F_{22} = 2.75$). The dotted lines show the generic case ($F_{11}/F_{22} = 2.8$) for that regime.* [47]

is not reached and instead a state with $\theta = \pi$ (except near the electrodes) is reached. In region III the Frederiks transition is first order like. Only in a very small parameter range the small amplitude and the large amplitude behavior are asynchronous. There the restabilization instability is still continuous, but the stabilized ground state is not reached (fig. 16), showing that the amplitude equation is qualitatively correct for most parameter values, but not really everywhere.

Since the fully nonlinear solutions are obtained only numerically, there would be some advantage for having an analytical model that reproduces the numerical results. The amplitude eqs. (36) are really 2 different equations (for each instability a separate one) so they cannot describe the full bifurcation scenarios. A suitable model is the following phenomenological amplitude equation

$$\partial_t A = \eta\,(1-\eta)\,A - g(\eta)\,A^3 - A^5\,, \tag{39}$$

which can be derived from a potential P via $\partial_t A = -\frac{\delta P}{\delta A}$.

$$P = \frac{1}{2}\left[\frac{1}{3}A^6 + \frac{1}{2}g(\eta)A^4 - \eta\,(1-\eta)A^2\right] \tag{40}$$

With the choice $g(\eta) = S\,(C-\eta)$ the three regimes I, II, and III are reobtained by $C > 1$, $0 < C < 1$, and $C < 0$, respectively. The fine-tuning can be done by choosing S. An example for the potential P in regime I is shown in fig. 17.

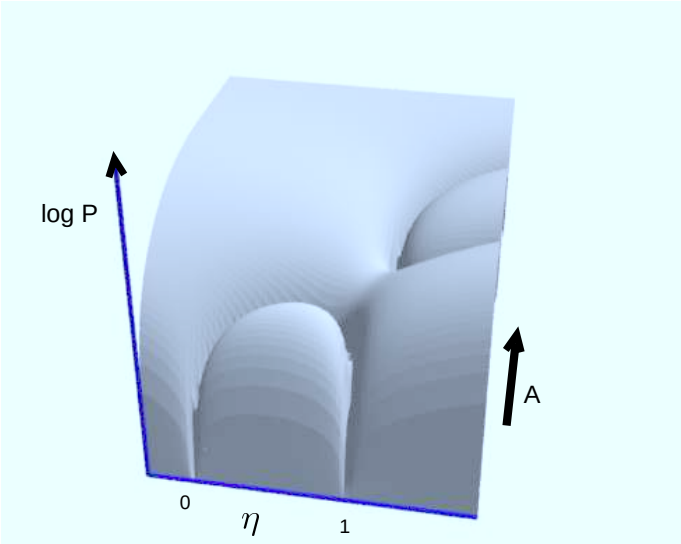

Figure 17: *Model potential P suitable for regime* I

3 Electroconvection Theory in Smectic C and Smectic C* Films

Most of the experimental and theoretical work on electroconvection (EC) in liquid crystals is devoted to nematic liquid crystals. This part has been reviewed in several works [2, 29, 30, 31, 32, 50]. In comparison rather little is known about electroconvection in smectic phases. Electroconvection observed in experiments on smectics so far is mainly driven by mechanisms which are rather independent of the Carr-Helfrich mechanism and the liquid crystalline symmetries. Some of those mechanisms usually work also in the isotropic phase of the material as described in more detail in sec. 4.1.

It is an interesting question which distinctive features of electroconvection might be related to the symmetries of smectic liquid crystals. Application of electric fields to a smectic C sandwich cell with the layers stacked perpendicular to the cell plane (as shown in fig. 18) can in principle induce convection structures driven by a mechanism similar to the Carr-Helfrich mechanism in the nematic phase. Figure 18 sketches a side view of such a cell with the smectic layers in bookshelf geometry. The $\boldsymbol{c}$ director, denoted by the arrows in the fig. 18, plays the same role here as the director $\boldsymbol{n}$ in the nematic phase. The $\boldsymbol{c}$ director is fixed at the glass plates but can reorient in the smectic layer plane.

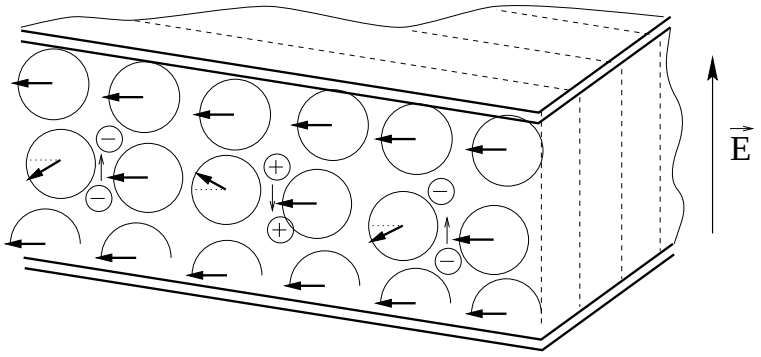

Figure 18: *Geometry of smectic* C *sandwich cell with electroconvection domains, layers in bookshelf geometry. The arrows denote the* $\boldsymbol{c}$ *director, the projection of the tilted director* $\boldsymbol{n}$ *onto the layer plane.*

Here we describe mechanisms for electroconvection which are specific for liquid crystals, in particular smectic C and smectic C* films. We do not discuss surface charge driven instabilities, because they are not specific to liquid crystals. Such mechanisms can be avoided using large parallel capacitor like electrodes. We restrict the theoretical formulation to fixed smectic layers (i.e. rigid film geometry $\mathfrak{T}_{ijkl} \to \infty$, $u = 0, v_z = 0$). It is also assumed that neighboring smectic layers behave equally, hence all gradients ∂_z vanish.

Under these conditions electroconvection in free standing smectic C films

is isomorphic to a two dimensional nematic liquid crystal. Investigations on this system are rather promising to gain further insight into the mechanism of electroconvection, because the motion can be visualized in more detail in a film.

As discussed in sec. 2.6 the SmC* is biaxial for film thicknesses small compared to the pitch. The number of coefficients contained in the material tensors such as the tensors for electric conductivity, for the dielectric tensor and elasticity is much larger than for nematic liquid crystals. However, this is neglected in the following consideration and a SmC* film is described being isomorphic to a two-dimensional nematic but with an additional spontaneous electric polarization $\mathbf{P}$, which is coupled rigidly to the in-plane director . The same geometry as in sec. 2.6 and in fig. 3 is considered.

3.1 Linear Equations

The stability of the convection–free, planar basic state $\mathbf{c} = (0, 1)$, $\mathbf{v} = 0$ and $\phi^{el} = 0$ is investigated in this section. To test the stability of this state, the equations of motion are linearized with respect to small deviations from it. Due to the 2D description there are no gradients in z–direction and all vectors have vanishing z–components (i.e. $v_z = 0$). The component v_y is expressed by v_x via the incompressibility condition.

After elementary algebraic operations, described in more detail in refs. [47, 48] one ends up with three coupled two–dimensional equations

$$\begin{aligned} 0 = & \left((\epsilon_1 \sin^2\psi + \epsilon_3)k_y^2 - \epsilon_3\nabla_x^2\right)\partial_t\phi^{el} + (-\epsilon_1 \sin\psi\, E_o(t) + p_0)\, k_y\, \partial_t n_3 \\ & + \left(\sigma_{yy}k_y^2 - \sigma_{xx}\nabla_x^2\right)\phi^{el} - \Big(\epsilon_1 \sin\psi\,(\,\partial_t E_o(t)\,) + \frac{\sigma_{yy} - \sigma_{xx}}{\sin\psi}\, E_o(t)\Big) k_y\, n_3\,, \end{aligned} \tag{41}$$

$$\begin{aligned} 0 = & -k_y\partial_t n_3 + (p_0 - \epsilon_1 \sin\psi\, E_o(t))\, k_y^2\, \phi^{el} - \left(\alpha_2 k_y^2 + \alpha_3\nabla_x^2\right)\, v_x \\ & + \left(\epsilon_1 \sin\psi\, E_o^2(t) - p_0\, E_o(t) - F_{11}\, k_y^2 + F_{22}\nabla_x^2\right)\, k_y n_3\,, \end{aligned} \tag{42}$$

$$\begin{aligned} 0 = & \rho_m(k_y^2 - \nabla_x^2)\,\partial_t v_x + \left(\eta_c\, k_y^4 - 2\,\hat{\eta}\, k_y^2\,\nabla_x^2 + \eta_b\,\nabla_x^4\right) v_x \\ & + k_y\left(\alpha_2 k_y^2 + \alpha_3\nabla_x^2\right)\partial_t n_3 + \left(\epsilon_1 \sin\psi\, E_o^2(t) - p_0 E_o(t)\right) k_y^3\, n_3 \\ & + \left(\epsilon_3\nabla_x^2 - (\epsilon_3 + \epsilon_1 \sin^2\psi)\, k_y^2\right)\, k_y^2\, E_o(t)\, \phi^{el}\,. \end{aligned} \tag{43}$$

Herein the following abbreviations for the viscosities have been used:

$$\begin{aligned} 2\,\alpha_2 &= -1 - \lambda^{(3)}\,, & 2\,\alpha_3 &= 1 - \lambda^{(3)}\,, \\ \eta_b &= \nu_3 + \frac{1}{4}\,(1 - \lambda^{(3)})^2\,, & \eta_c &= \nu_3 + \frac{1}{4}\,(1 + \lambda^{(3)})^2\,, \\ \hat{\eta} &= \frac{1}{\gamma_1}(\nu_1 + \nu_2 - \nu_3) + \frac{1}{4}(1 - \lambda^{(3)^2}), \end{aligned} \tag{44}$$

where the ν's are ordinary viscosities [43], while $\lambda^{(3)}$ is a reactive transport parameter [51]. These equations can be rescaled and reformulated in dimensionless form as discussed in ref. [48]. They are similar to the linear equations

for planarly aligned nematic liquid crystals [26, 48, 52], but contain in addition the effects of the polarization p_0. Accordingly, the eqs. (41-43) have a different symmetry, which is described in more detail in sec. 3.3. They can be written in a more compact matrix form,

$$\mathsf{B}(t, \nabla_x) \cdot \partial_t \boldsymbol{U}(x,t) = \mathsf{L}(t, \nabla_x) \cdot \boldsymbol{U}(x,t)\,, \tag{45}$$

with the (formal) vector field,

$$\boldsymbol{U} = (\phi^{el}, \theta, v_x). \tag{46}$$

Either DC or periodic AC driving voltages are assumed in the following. For periodic voltages $V(t) = V(t+T)$, with $T = 2\pi/\omega$, the matrices B and L are periodic in time and eq. (45) shares some similarities with the well known Mathieu equations. In the following we assume additionally

$$V(t + T/2) = -V(t). \tag{47}$$

3.2 Boundary Conditions

A specification of the boundary conditions is needed when the linear equations (41-43) are analyzed. Usually films are considered which are infinitely extended in y-direction (or take periodic boundary conditions). In x-direction the film is confined between electrodes located at $x = \pm\frac{1}{2}$, with the consequence that the velocity v_x, perpendicular to the electrodes, has to vanish at this surface

$$v_x(\pm\frac{1}{2}) = 0\,. \tag{48}$$

In addition either stress-free or rigid boundary conditions

$$\partial_x^2 v_x(\pm\frac{1}{2}) = 0\,, \qquad \partial_x v_x(\pm\frac{1}{2}) = 0\,, \tag{49}$$

are assumed, where the latter case is closer to real experimental conditions.

The induced potential has to be zero at the surface and for the director $\boldsymbol{c}$ we consider planar boundary conditions ($\boldsymbol{c} = (0,1)$)

$$\theta(\pm\frac{1}{2}) = 0\,, \qquad \phi^{el}(\pm\frac{1}{2}) = 0\,. \tag{50}$$

3.3 Symmetries and Floquet Analysis

The solutions of the linearized eqs. (45) can be classified with respect to their symmetry properties under spatial reflections and translations in time. Choosing the line $x = 0$ to be the middle of the film, i.e. $-1/2 < x < 1/2$, where 1 is the rescaled film width in fig. 3, eq. (45) is invariant under reflection with respect to $x \to -x$.

This symmetry of the equations, together with the boundary conditions chosen, allows to characterize all solutions to be either symmetric, $\boldsymbol{U}(x) =$

$\boldsymbol{U}(-x)$, or antisymmetric, $\boldsymbol{U}(x) = -\boldsymbol{U}(-x)$, with respect to x. For periodic voltages that fulfill eq. (47), the linear homogeneous eq. (45) is invariant under time translations

$$t \to t + nT \qquad (n \text{ integer, positive}) \,. \tag{51}$$

According to the spectral method of Floquet [53] this leads to a general solution of the form,

$$\boldsymbol{U}(z,t) = \hat{\boldsymbol{U}}(z,t)e^{\sigma t} \,, \tag{52}$$

with the Floquet exponent σ and the periodic function $\hat{\boldsymbol{U}}$. Due to the symmetry (51) the solutions $\hat{\boldsymbol{U}}$ are grouped according to the integers n into harmonic ones ($n = 1$) and subharmonic ones ($n = 2$). The harmonic ones are invariant under a single T-translation $t \to t+T$, i.e. $\hat{\boldsymbol{U}}(t) = \hat{\boldsymbol{U}}(t+T)$, while the subharmonic ones change sign $\hat{\boldsymbol{U}}(t) = -\hat{\boldsymbol{U}}(t+T)$ under that translation. The full solutions $\boldsymbol{U}(t)$ do not have these symmetries because of the Floquet multiplier $\exp(\sigma t)$. However, the prefactor produced by a time translation, i.e. $\exp(\sigma T)$ for a T-translation, is irrelevant, since the amplitude of a solution $\boldsymbol{U}(t)$ is not determined by the linear, homogeneous equation (45).

The Floquet exponent σ is a function of the external (V_0, ω) and internal (material) parameters of the system and depends on the transverse wave vector k_y. It governs the linear stability of the basic, non-convective state against inhomogeneous perturbations, which is stable, if $Re(\sigma) < 0$, and unstable for positive growth rates $Re(\sigma) > 0$. Thus, from the condition,

$$Re\left[\sigma(V_0, k_y, ...)\right] = 0 \,, \tag{53}$$

those parameter values are determined, which separate the linear stable regime from the unstable one. Equation (53) allows for instance the determination of V_0 as a function of k_y, the so called neutral curve, $V_0(k_y)$, at which the real part of the Floquet exponent changes its sign. The absolute minimum of $V_0(k_y)$ at a critical k_{yc}, $V_c = V_0(k_{yc})$, gives the threshold for the onset of convection in linearized stability analysis.

For vanishing p_0 (SmC phase) and if additionally eq. (47) holds, e.g. the driving voltage is sinusoidal, or of square or triangular wave form, there is an additional symmetry with respect to time translations, since eq. (45) is invariant under the replacement,

$$t \to t + \frac{T}{2}, \quad \text{if} \quad \begin{pmatrix} \phi^{el} \\ \theta \\ v_x \end{pmatrix} \to \pm\gamma \begin{pmatrix} -\phi^{el} \\ \theta \\ v_x \end{pmatrix} \,, \tag{54}$$

where γ is an irrelevant constant. This symmetry requires the solutions $\hat{\boldsymbol{U}}$ to be harmonic, since by applying (54) twice (i.e. after a T-translation) $\hat{\boldsymbol{U}}$ is mapped to itself. Thus, if eq. (54) is valid, subharmonic solutions are ruled out. The upper and lower sign in (54) belong to two different solutions, corresponding to the so-called conductive and dielectric regime, respectively,

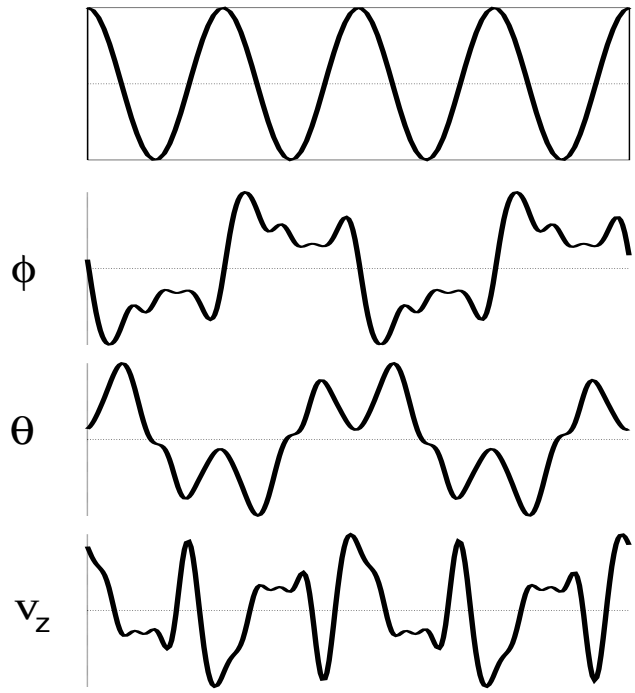

Figure 19: *The time dependence of the field variables is shown at the onset of EC in the SmC* phase (with macroscopic polarization). The fields at the cell center ($x = 0$) are plotted in arbitrary units for the frequency $\omega = 390$ of the applied voltage. The dynamics of the system is $2T$-periodic only, although the driving force $E_0(t)$ is T-periodic* [48].

known from EC in nematic liquid crystals [1]. In SmC* however, this symmetry (54) is lifted, since $p_0 \neq 0$. In that case subharmonic solutions are possible (fig. 19) and the two harmonic regimes – although still discernible – are no longer purely "conductive" nor purely "dielectric". This is discussed in more detail in sec. 3.5.

3.4 Onset of Convection for DC Voltage

As for the polarization Frederiks transition described in sec. 2.6, the existence of a finite polarization in the SmC* phase has also a profound influence on the DC electroconvective instability. Without a polarization p_0, as in the smectic C phase, the sign of the DC voltage is arbitrary and the threshold for the DC electroconvection depends on V_0^2 only. This behavior is changed by the presence of the polarization $\mathbf{P}$ in SmC*. Now $\mathbf{E}$ parallel to $\mathbf{P}$ ($V_0 > 0$) is energetically preferred to the case $\mathbf{E}$ antiparallel to $\mathbf{P}$ ($V_0 < 0$) (cf. fig. 3) indicating that the basic state is more stable in the former situation than in the latter one. Thus, one can expect the DC electroconvection threshold to increase (decrease) with p_0 for $V_0 > 0$ (< 0), which indeed has also been found

numerically for rigid boundaries [48].

This can be understood analytically as well. Assuming stationary instabilities (a Hopf bifurcation has not been found in our studies), we get a quadratic equation for $V_0(q)$, i.e. $b_1 V_0^2 + b_2 p_0 V_0 + b_3 = 0$, which is written down explicitly for the special case $\epsilon_a = 0$ and stress-free boundary conditions in ref. [48]. The interesting point is that the linear term of the polynomial is proportional to p_0. Thus, in contrast to the smectic C case, in the smectic C* phase the neutral curve for DC EC is no longer symmetric w.r.t. $V_0 \to -V_0$.

This simple threshold condition also explains, why for finite values of p_0 the range of existence of the DC electroconvection is larger than for zero p_0. Real values for V_c are only possible, if $p_0^2 b_2^2 > -4 b_1 b_3$. Thus, for zero p_0 the product $b_1 b_3$ must be negative, while for large enough p_0 also positive values of $b_1 b_3$ lead to an instability threshold. In particular, for a large enough and destabilizing polarization ($\mathbf{E}$ antiparallel to $\mathbf{P}$, $V_0 < 0$), an electroconvective instability is possible, even if $\epsilon_1 (= \epsilon_a) \leq 0$ and $\sigma_1 (= \sigma_a) = \sigma_{yy} - \sigma_{xx} < 0$. In this situation the planar basic state is stable within the simple Carr-Helfrich mechanism ($p_0 = 0$), but the destabilization due to p_0 overcomes the stabilization due to negative dielectric and conductive anisotropies. An interesting competition between the static Frederiks transition and the EC may be found, as discussed in more detail in ref. [48].

3.5 Onset of Convection for AC Driving Voltage in SmC* Films

For an AC driving voltage, in the smectic C phase ($p_0 = 0$) the harmonic solutions (cf. sec. 3.3) are each decomposed into two independent classes (called A and B in [50, 52]) representing the conductive and dielectric regime, respectively. These two regimes are well known from EC in nematic liquid crystals [1, 30, 32]. Hence SmC liquid crystals are isomorphic to two-dimensional nematics in the present approximation.

The presence of the finite polarization in SmC* allows, in addition, for a subharmonic ($2T$-periodic) solution (figs. 19, 20, 21), thus breaking spontaneously the discrete time translational symmetry of the (T-periodic) driving voltage. The subharmonic regime is strictly prohibited, if the symmetry (54) holds.

For finite polarization, besides the neutral curves for the (former) conduction and the (former) dielectric regime, an additional neutral curve for the subharmonic regime arises at intermediate frequencies, as is shown in fig. 20. The former conductive and dielectric regime are shifted by the polarization. Changing the frequency ω the three minima of the neutral curve in fig. 20 are shifted relative to each other, such that any of them, can be the absolute minimum, i.e. the threshold V_c for a certain frequency range. The critical threshold voltages, $V_c(\omega)$ and the associated critical wave vectors $k_{yc}(\omega)$ are plotted for each regime as a function of frequency ω in fig. 21 for two different values of the polarization p_0.

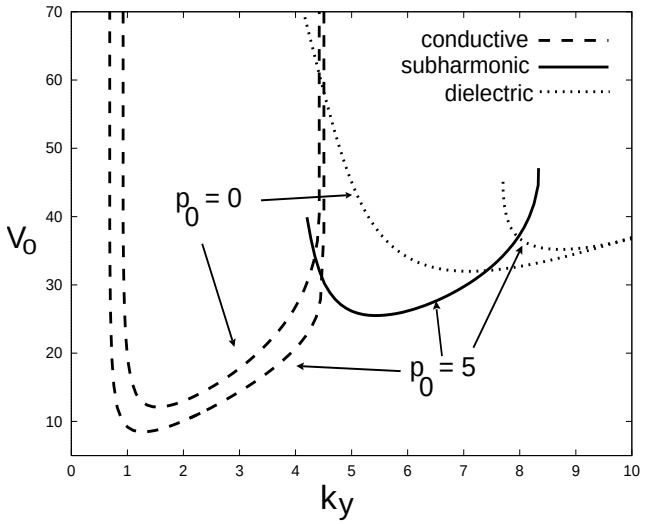

Figure 20: *Neutral curves $V_0(k_y)$ are shown for two different values of the polarization ($p_0 = 0$ and 5 according to the arrows) at a fixed frequency ($\omega = 180$) of the applied voltage. The conduction regime (dashed lines) and the dielectric regime (dotted lines) are present for any p_0. Only for finite polarizations the additional subharmonic regime occurs at intermediate k_y values (solid line).*

For sufficiently high values of p_0 the neutral curve belonging to the subharmonic regime has the lowest minimum for a certain frequency range (solid line in fig. 21). It always appears at intermediate frequencies, between the conductive and dielectric regime. Figure 21b shows the critical wavenumber k_{yc} as a smooth function of the external frequency within a given regime, but with discontinuous jumps when the marginal stability switches from one regime to another. Again only two regimes are present for $p_0 = 0$, but three for large enough p_0. Although there is no simple mechanism that could explain, why a subharmonic regime exists as the marginally stable solution, the following remarks may help the intuition. With $p_0 = 0$ the sign of V_0 is undefined and it is rather V_0^2 that governs the instability thresholds. A finite p_0, however, introduces contributions linear in V_0 as has been shown explicitly in the DC case (sec. 3.4). Thus for sinusoidal voltages $V(t)$ the fields may oscillate either with half the frequency of $V(t)^2$ or $V(t)$, depending on the influence of the different destabilizing forces. For very large threshold voltages, such as in the dielectric regime, contributions in the director relaxation time being quadratic in the voltage, V^2, win over those effects linear in V. At small frequencies in the conduction regime the threshold is relatively small and the impurity charges can follow the action of the external field immediately while leaving the director orientations roughly unchanged. In both cases the fields oscillate in a subharmonic fashion with respect to V^2.

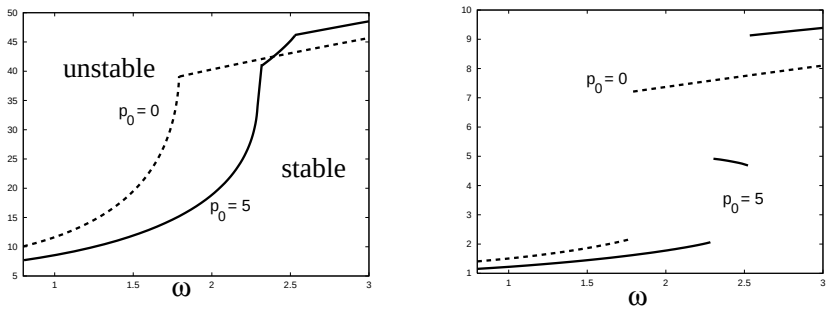

Figure 21: *Onset of instability: The critical voltages $V_c = V(k_{yc})$ (left) the critical wavelengths k_{yc} (right) of the three regimes as a function of the applied AC frequency. For low or vanishing polarization p_0 there are only two regimes, while for $p_0 > 4.5$ (for the parameters chosen) there is in addition the subharmonic regime at intermediate frequencies. At those frequencies, where the instability switches from one regime to the other, the critical wave vector shows a jump* [48].

The frequency range of the conduction regime is always bounded from above by the inverse charge relaxation time. Beyond that frequency the charges cannot follow the external field. If immediately beyond that frequency the contribution $p_0 V$ to the director relaxation time is more important than those proportional to V^2, then the subharmonic regime may have a lower threshold than the dielectric one. With further increasing frequency also the threshold increases, and therefore at large frequencies V^2 dominates the V effect and the dielectric regime is favored. Using these qualitative arguments the subharmonic regime can only occur as an additional regime between the conduction and the dielectric regime.

3.6 Codimension-3 Bifurcation

The value of p_0 can be seen as a third control parameter of the system in addition to the amplitude, V_0, and frequency, ω, of the applied voltage. For large polarizations the subharmonic threshold curve $V_c(\omega)$ intersects both, the conductive and the dielectric threshold curve, at two codimension-2 points (indicated in fig. 21). If p_0 is lowered, these two codimension-2 points approach each other and finally merge (cf. fig. 22). We have found numerically that this coalescence happens just at the point, where also the conductive and dielectric thresholds intersect. Here all three regimes coexist and a competition of three solutions having different wavelengths should be seen in experiments. For $p_0 < p_3$, the subharmonic regime disappears. (The actual value of p_3 depends obviously on the material parameters.) This scenario seems to be generic, since near this codimension-3 point the threshold curves $V_c(\omega)$ are

nearly straight lines, where the conductive and dielectric curve have the largest and smallest slope, respectively. Increasing however the polarization p_0 well

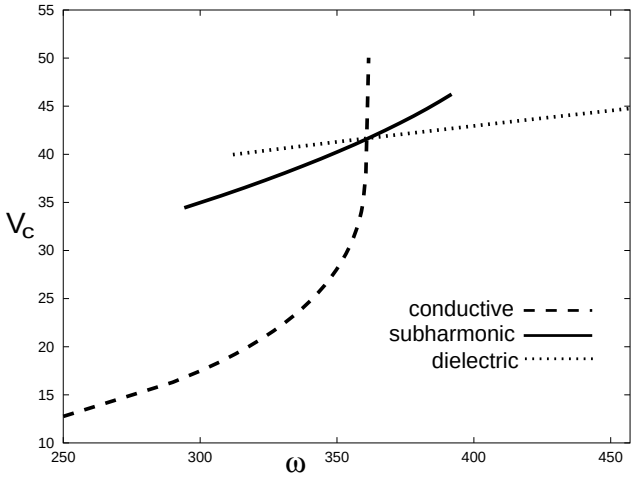

Figure 22: *Codimension-3 point: At the minimal value of the polarization ($p_0 = 4.5$ for the parameters chosen), for which the subharmonic regime exists, the three different regimes have equal critical voltages at a certain external AC frequency $\omega_3 \approx 361$. This is a codimension-3 point* [48].

beyond p_3 the cutoff frequency of the conductive regime is shifted to higher values and the threshold and critical wavelength at a fixed frequency is lowered further. The subharmonic regime appears always after the cutoff of the conductive regime for high values of p_0 and is extended to much higher frequencies at the cost of the dielectric regime. For large polarizations p_0 in the conductive regime we find typically rather small threshold values $k_{yc} \approx 0.15$ and $V_c \approx 0.5$ at $\omega = 200$. The observation of such very small wavenumbers should not be confused with the Frederiks transition ($k_y \equiv 0$, which does not occur for $\epsilon_1 < 0$).

3.7 Parameter Dependencies

The frequency range, where the subharmonic regime has the lowest threshold, depends not only on the polarization but also on the values of the other material parameters and on the film width. To design an experiment for investigating the subharmonic regime it is helpful to know, for which geometric and material parameters the subharmonic regime can be observed most likely. All results described in the previous sections of this work have been calculated for the values given in Appendix A of ref. [48]. The electroconvective instability is especially sensitive to changes in the electrical anisotropies $\epsilon_a = \epsilon_1$ and $\sigma_a = \sigma_{yy} - \sigma_{xx}$ [25, 26, 50, 52]. Therefore we consider the influence of variations of these quantities on the existence range of the subharmonic regime.

As an example the dependence on σ_a has been investigated by keeping σ_{xx} constant and changing the value of σ_{yy}. Increasing values of σ_a enforce the ability of space charges to follow the applied alternating field up to higher frequencies according to the Carr-Helfrich mechanism [1, 19]. Thus the cut-off frequency of the conductive regime increases approximately proportional to σ_a while the dielectric regime is only slightly affected. This is shown for $p_0 = 0$ by the dashed line in fig. 23. Similar behavior is found for a finite polarization (solid lines) although for $\sigma_a/\sigma_{xx} < 0.55$ (for the parameters chosen) the subharmonic regime squeezes in between the two other regimes. The threshold voltages of the conductive and the dielectric regimes diverge by approaching $\sigma_a \to 0$ according to the Carr-Helfrich mechanism causing smaller values of the anisotropy σ_a to favor the subharmonic regime. Furthermore the subharmonic regime exists even for (slightly) negative values of the anisotropy σ_a. The same has been found for an applied DC-voltage (sec. 3.4). Increasing p_0 will again lead to a larger frequency range of the subharmonic instability and the subharmonic regime will exist to even larger values of σ_a than indicated in fig. 23.

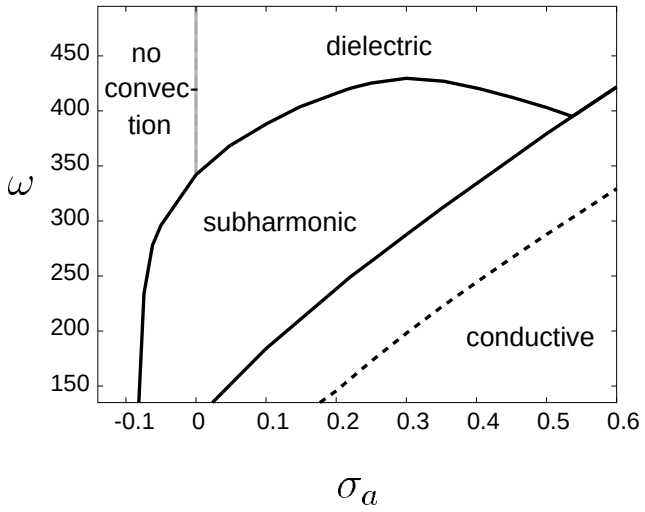

Figure 23: *The solid lines indicate the existence ranges of the different instability regimes at various AC frequencies as a function of the conduction anisotropy σ_a for $p_0 = 5$ and $\sigma_{xx} = 133$ and $\epsilon_x = 5.25$; $\epsilon_a = -0.38$. The dashed line describes the codimension-2 line between the conductive and the dielectric regimes for $p_0 = 0$.*

Another interesting dependence, the dependence of variations on the film width has also been discussed in ref. [48].

4 Electroconvection Experiments on Smectic Films

4.1 General

When pattern formation by electroconvection in freely suspended smectic films is discussed, at least three different mechanisms have to be considered. The first type of instability bases on the Carr-Helfrich mechanism known from nematic liquid crystals. Here an in-plane anisotropy of the conductivity is required, which is present in the tilted smectic C and C* phases, but not in the A phase. A modification of this mechanism by an additional polarization **P** has been discussed theoretically in the previous section.

A second mechanism works via charge injection at the electrodes and has been reported for isotropic liquids already in 1936 [54]. Since then this instability has been studied in a variety of systems (e.g. [55, 56, 57, 58, 59]). Another mechanism is due to surface charge layers ("diffusion layers") [60, 61, 62]. These different mechanisms in general do not necessarily exclude each other, a competition or interplay of them is very likely in smectic films. In some cases, the special choice of substances or experimental conditions may allow a separate study of the individual effects.

In the first experiments reported on electroconvection in freely suspended films nematic liquid crystals have been used [60, 61]. Faetti and his coworkers used the nematic liquid crystal 4-n-butyl-N-(4-methoxybenzylidene)-aniline (MBBA). The nematic director in these films is anchored at the liquid crystal-air interface at some small angle with respect to the film normal. An electric field applied parallel to such films leads to characteristic convection vortices which can be visualized in the optical transmission texture.

Faetti et al. discovered two different convection modes in their nematic films. In thin layers, the threshold for onset of electroconvection depends linearly on the film thickness. For an explanation of this so-called *vortex mode* (VM) the authors developed a model which bases on the interactions of surface charges on the film with the electric field. This vortex mode occurs also in the isotropic phase of a material and therefore the Carr-Helfrich mechanism could be excluded as the driving effect. Moreover, the experiments were also performed with insulated and conducting electrodes to exclude convection driven by charge injection.

With increasing film thickness, the threshold for the vortex mode increases and consequently the authors observed the crossover to a different convection type [60] in thick films (several micrometers). The threshold voltage of this structure, the so-called *domain mode* (DM), is independent of the film thickness. This regime is driven by bulk charges and two frequency regimes of convection have been observed for AC electric fields, similar as in electroconvection in nematics between two glass plates. Accordingly the domain mode has been also explained by the Carr-Helfrich mechanism.

The latter is characterized by an oscillating charge field at low frequencies and another at high frequencies with oscillating director field. The viewing

direction in the geometry of nematic films is into the rolls, in contrast to conventional nematic sandwich cells. In the isotropic liquid phase, only the vortex mode remains, the domain mode requires the anisotropic electric properties of the nematic phase.

4.2 Experiments on Freely Suspended Smectic A Films

In isotropic liquids and nematic phases a molecular layer structure as in smectic liquid crystals is absent. Therefore such nematic films are unstable, their thickness is inhomogeneous and subject to considerable fluctuations and their lifetime is restricted. Moreover, the velocity field is very complex and not necessarily restricted to a two-dimensional flow.

In contrast, the layer structure of smectics guarantees well-defined homogeneous film thickness and the flow takes place essentially in planes of the smectic layers. Morris and coworkers [40, 41] investigated free-standing smectic A films under lateral electric fields and discovered a vortex mode analogous to the nematic phase. Faetti's theoretical explanation which is independent of the anisotropy in the smectic layers, was adapted to smectic films and developed further. Analytical expressions for the threshold voltage of vortex electroconvection has been derived by Daya et al. [62]

$$U_c = \frac{d_z}{\epsilon_0} \sqrt{\sigma \eta R_c} \; . \tag{55}$$

σ is the in-plane electric conductivity, η is the viscosity of the smectic material, d_z is the film thickness and R_c denotes a constant, which depends on the electrode shape. Plate electrodes with $R_c \approx 92$ and wire electrodes with $R_c \approx 77$ lead to slightly different threshold fields. Characteristic for the vortex electroconvection is the linear dependence of the onset voltage on film thickness, which is confirmed very well in experiments. Smectic A films are isotropic within the layers. Hence, the Carr-Helfrich mechanism does not work in these materials. For this isotropic mechanism in smectic A the theory has been also extended recently by a perturbation calculation into the weakly nonlinear regime [63].

4.3 Experiments on Freely Suspended Smectic C Films

Electroconvection in smectic C films has been studied quite recently in experiments by Becker et al. [64] and Langer et al. [65, 66]. The principal difference to the smectic A phase is the in-plane anisotropy. With polarizing microscopy, a flow induced optical texture (SmC *schlieren*) can be observed. Vortex flow in the smectic C phase can be immediately traced from the texture changes in the optical reflection or transmission image. Two effects are superimposed, the first is a texture transport by the mass flow in the film plane. The second effect is the reorientation of the $\boldsymbol{c}$ director by flow coupling, in an inhomogeneous flow field, a hydrodynamic torque acts on $\boldsymbol{c}$. Figure 24 shows typical convection textures in a smectic C film driven at low frequency AC (polarized

light, no analyzer). Between adjacent dark and bright stripes, the $\boldsymbol{c}$-director is rotated by 90°.

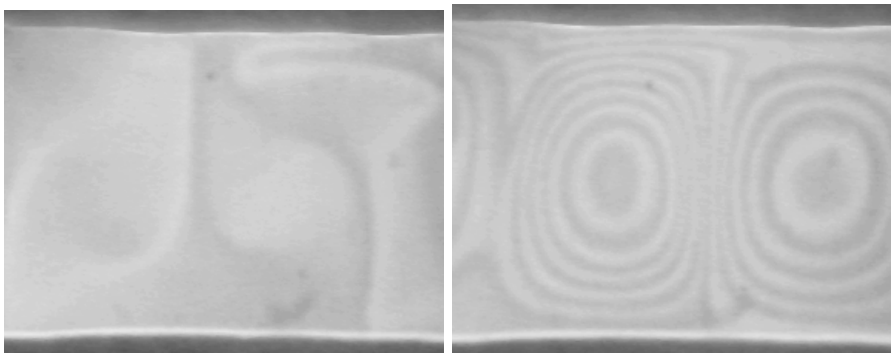

Figure 24: *Reflection texture of* EC *vortices in a smectic* C *film. The electrodes are at the upper and lower edges, with 0.55mm gap. Vortices appear at 22V and 0.5Hz (left), while ring structures are seen at the field reversal (30V) and 0.3Hz (right).*

At DC excitation the flow is unidirectional, the director walls are carried with the flow field and wind up to spirals until the counter-action of increasing elastic deformations establishes a stationary asymptotic state of the director fields.

At AC excitation, the director walls wind up during one half cycle (fig. 24 left) but the flow is reversed in the next half cycle. The right image in fig. 24 shows the moment of field reversal, where the walls have formed a concentric ring system. When threshold fields for convection are measured in dependence upon the film thickness, a qualitative and quantitative correspondence with the vortex mode in SmA is found [66]. Also for a smectic C mixture, the threshold increases rather linearly with the film thickness as shown in fig. 25. This indicates that the observed pattern in SmC is of the same type as the vortex convection found in smectic A films. It is driven by surface charges and decorated by the texture flow. The deformation of the $\boldsymbol{c}$-director field by the flow field is huge, while in the opposite direction the influence is negligibly small. In the smectic C material, in principle a Carr-Helfrich type of convection could occur as discussed in sec. 3, but the surface driven vortex flow effects have been suppressed. In these experiments on SmC the vortex mode has obviously a lower threshold field. Carr-Helfrich driven convection is conceivable only at high frequencies or in very thick films ($d_z \gg 1\mu m$). A cross-over between both types as detected in nematic films [61] has not yet been described for smectics.

4.4 Electroconvection in smectic C* films

Electroconvection in ferroelectric smectic C films have been performed so far only in materials with high spontaneous polarization $\boldsymbol{P}$ [66]. In this material,

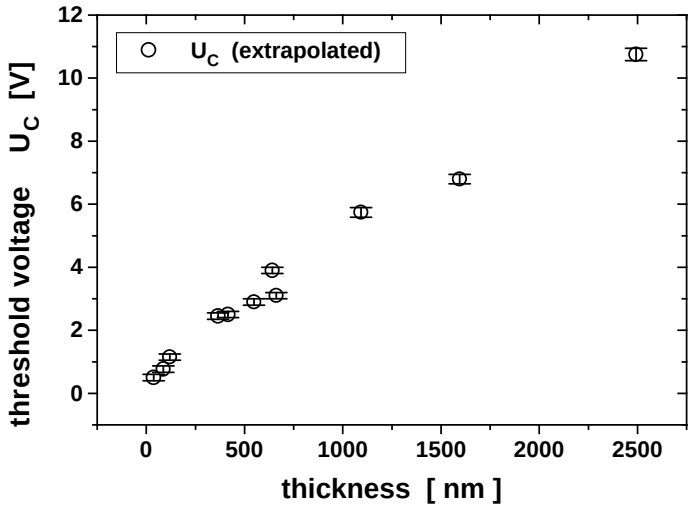

Figure 25: *Onset voltage for electroconvection in a smectic* C *mixture in dependence of the film thickness* d_z *(50% 5-n-Octyl-2-(4-n-hexyloxyphenyl)-pyrimidin and 50% 5-n-Octyl-2-(4-n-octyloxyphenyl) -pyrimidin with phase sequence* $< -10°C$ S_C $50.5°C$ S_A $53°C$ N $68°C$ I*, electrode gap 0.5mm ,* T*=25° C,* $\sigma = 8.92 \cdot 10^{-12} A/(Vm)$) [66]

the interaction of $\boldsymbol{P}$ with the external electric field $\boldsymbol{E}$ is dominant. The $\boldsymbol{c}$ director aligns perpendicular to $\boldsymbol{E}$. A convective vortex flow leads to periodic deflections of the $\boldsymbol{c}$ director from its fixed alignment but is too weak to create disclination walls. The vortices are visualized with crossed polarizers slightly oblique to the electrode geometry which decorates oppositely rotating vortices with different reflection intensities. Figure 26 shows the reflection texture of a 2.1 μm thick film in the SmC* phase observed with crossed polarizers. A small angle $< 20°$ was adjusted between the electrode and the polarizer. The oppositely rotating vortices are visible as rectangular areas of nearly uniform brightness.

In the SmC* films one observes DC electroconvection already at very low voltages. Figure 27 gives the flow velocity as a function of the applied voltage. Note that the onset threshold in SmC was 0.5V even in the thinnest films. For SmC* a non-zero critical voltage cannot be derived from these experiments, it is below the experimental resolution. Moreover, it is characteristic that the convective flow velocity is independent of the film thickness d_z. This indicates that the convection in these films is not primarily driven by the film surface.

The interpretation of these observations is not unambiguous. On the one hand, many arguments characterize the observed effect as a Carr-Helfrich type convection as predicted in ref. [48], cf. sec. 3. The well defined ground state with the $\boldsymbol{c}$ director parallel to the electrode edges exists, the periodic director deflection is small ($\ll 90°$) and the observed flow velocity is film thickness independent over a large thickness range. The flow field itself is very similar

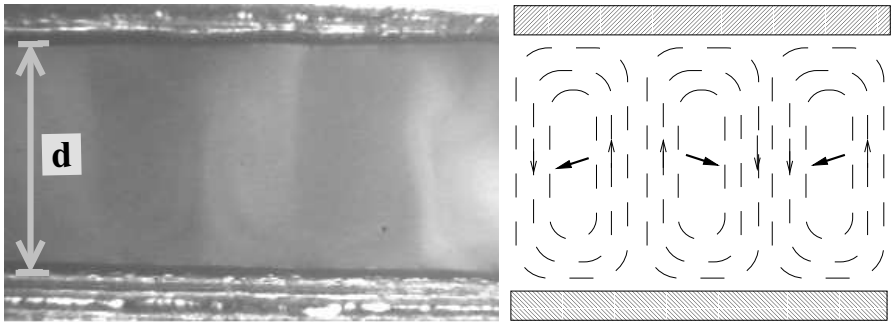

Figure 26: *Reflection texture of* EC *in a smectic* C* *film ($d_z = 2.1\mu m$), with electrode gap 0.5mm, DC voltage 60V and crossed polarizers slightly rotated out of the electrode direction.* [67]

to that in the surface driven structures in SmA and SmC. A direct proof for or against one of both mechanisms has not yet been achieved (cf. the nematic films where a clear crossover between both mechanisms can be observed).

Experiments with AC electric fields can elucidate more of the driving mechanisms. However, in the ferroelectric smectic films the electroconvection is disturbed by the switching of the $\boldsymbol{c}$ director at field reversal, it reorients by 180° as the spontaneous polarization aligns with the external field $\boldsymbol{E}$. The disturbance of the EC vortices by ferroelectric switching is small only at very low frequencies (a few Hz). In these experiments one observes that the vortices change their sense of rotation with the driving field. Speaking in terms of the Carr-Helfrich mechanism, this means that the charges remain at their positions while the director reverses sign with the external field, this is characteristic for the so-called dielectric regime in EC of nematics (cf. also sec. 3.5).

Finally we summarize the progress made in the study of electroconvection in thin quasi two-dimensional films and sketch the perspectives of future work. The investigation of freely suspended films of tilted smectic phases has revealed new electroconvection scenarios and to a certain extend it has improved understanding of the electrohydrodynamic effects, but there are still many problems to be solved before a comprehensive description will be obtained. Theory and experiment are still a few steps apart, it should be a goal of future experimental investigations to prepare very low $\boldsymbol{P}$ ferroelectric samples, and an important theoretical task will be the combination of works in refs. [62, 48], which should include both surface effects and an in-plane electric anisotropy of the smectic material. In view of the many potential applications of ferroelectric smectics the understanding of electroconvection effects in these materials is not only of pure academic interest.

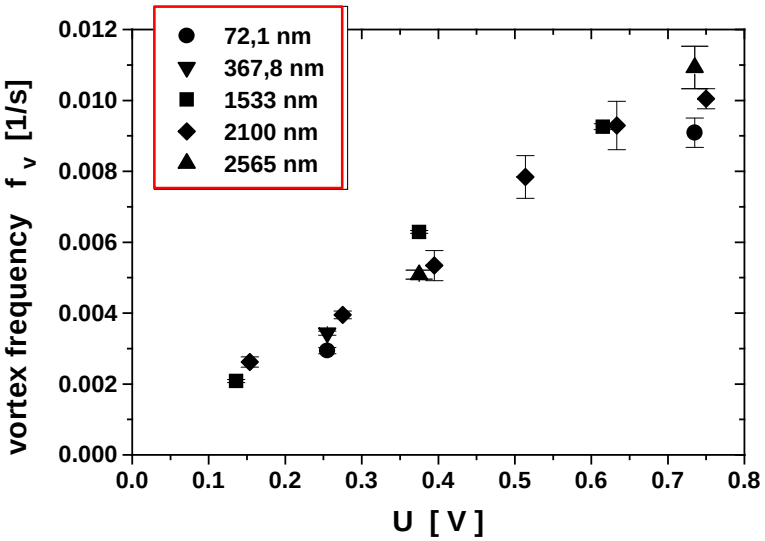

Figure 27: *Vortex velocity of convective flow in an* SmC* *film (ZLI 4237-100,* Merck*); films of different thickness d_z are compared (gap width 0.5mm, T=25° C).* [65]

Acknowledgement

H.P. and W.Z. thank S. Ried, on whose PhD thesis ([47]) sec. 2 is based, and H.R. Brand for valuable discussions. R.S. thanks Christian Langer for experimental data and the preparation of figures, W. Weissflog for synthesis of the SmC material and Stephen Morris for valuable discussions. This work has been supported by the Deutsche Forschungsgemeinschaft through Schwerpunkt "Strukturbildung in dissipativen kontinuierlichen Systemen – Experiment und Theorie im quantitativen Vergleich".

References

[1] P. G. de Gennes and J. Prost, *The Physics of Liquid Crystals* (Clarendon, Oxford, 1993).

[2] L. M. Blinov, *Electro-optical and magneto-optical properties of liquid crystals* (John Wiley, New York, 1983).

[3] M. C. Cross and P. C. Hohenberg, Rev. Mod. Phys. **65**, 851 (1993).

[4] *Spatio-Temporal Patterns in Nonequilibrium Complex Systems*, Vol. XXI of *Santa Fe Institute Studies in the Sciences of Complexity*, edited by P. Cladis and P. Palffy-Muhoray (Addision-Wesley, New York, 1995), .

[5] *Pattern Formation in Liquid Crystals*, edited by A. Buka and L. Kramer (Springer, Berlin, 1996).

[6] B. Bahadur, *LIQUID CRYSTALS, Applications and Uses* (World Scientific, Singapore, 1993).

[7] V. Frederiks and V. Tsvetkov, Sov. Phys. **6**, 490 (1934).

[8] W. Helfrich, Appl. Phys. Lett. **17**, 531 (1970).

[9] J. P. Hurault, J. Chem. Phys. **59**, 2068 (1973).

[10] A. Rapini, J. Phys. (Paris) **33**, 237 (1972).

[11] M. Hareng, S. L. Berre, and J. J. Metzger, Appl. Phys. Lett. **27**, 575 (1975).

[12] C. Y. Young, R. Pindak, N. A. Clark, and R. B. Meyer, Phys. Rev. Lett. **40**, 773 (1978).

[13] C. Rosenblatt, R. B. Meyer, R. Pindak, and N. A. Clark, Phys. Rev. A **21**, 140 (1980).

[14] P.E. Cladis, Y. Couder, and H.R. Brand, Phys. Rev. Lett. **55**, 2945 (1985).

[15] W. Zimmermann, S. Ried, H. Pleiner, and H. R. Brand, Europhys. Lett. **33**, 521 (1996).

[16] R. Williams, J. Chem. Phys. **39**, 384 (1963).

[17] A. P. Kapustin and L. S. Larionova, Kristallografiya **14**, 741 (1964).

[18] E. F. Carr, E. A. Hoar, and W. T. McDonald, J. Chem. Phys. **9**, 297 (1968).

[19] W. Helfrich, J. Chem. Phys. **51**, 4092 (1969).

[20] E. Dubois-Violette, P. G. deGennes, and O. Parodi, J. Phys. (Paris) **32**, 305 (1971).

[21] P. A. Penz and G. W. Ford, Phys. Rev. A **6**, 414 (1972).

[22] S. Kai and K. Hirakawa, Prog. Theor. Phys. Suppl. **64**, 212 (1978).

[23] A. Joets and R. Ribotta, in *Cellular Structure in Instabilities*, edited by J. E. Wesfreid and S. Zaleski (Springer, Heidelberg, 1984).

[24] R. Ribotta, A. Joets, and L. Lei, Phys. Rev. Lett. **56**, 1595 (1986).

[25] W. Zimmermann and L. Kramer, Phys. Rev. Lett. **55**, 402 (1985).

[26] E. Bodenschatz, W. Zimmermann, and L. Kramer, J. Phys. (Paris) **49**, 1875 (1988).

[27] I. Rehberg, S. Rasenat, and V. Steinberg, Phys. Rev. Lett. **62**, 756 (1989).

[28] S. Kai and W. Zimmermann, Prog. Theor. Phys. Suppl. **99**, 458 (1989).

[29] W. Zimmermann, Mat. Res. Bulletin **16**, 46 (1991).

[30] L. Kramer and W. Pesch, Annu. Rev. Fluid Mech. **27**, 515 (1995).

[31] L. Kramer and W. Pesch, in *Pattern Formation in Liquid Crystals*, edited by A. Buka and L. Kramer (Springer, Berlin, 1996).

[32] U. Behn and W. Pesch, Electroconvection in nematic liquid crystals, this volume, 1998.

[33] F. Aliev and K. F. Abbasov, Sov. Phys. Kristallogr. **30**, 442 (1985).

[34] J. P. Petrov, A. G. Petrov, and G. Pelzl, Liquid Crystals **11**, 865 (1992).

[35] A. B. Davey and W. A. Crossland, Mol. Cryst. & Liq. Cryst. **263**, 2267 (1995).

[36] L. K. Vistin and A. P. Kapustin, Kristallografiya **13**, 349 (1968).

[37] A. L. Bermain, E. Gelerinter, and A. de Vries, Mol. Cryst. & Liq. Cryst. **33**, 55 (1976).

[38] P.E. Cladis and H.R. Brand, Liquid Crystals, **14**, 1327 (1993).

[39] P.E. Cladis, P.L. Finn, and H.R. Brand, Phys. Rev. Lett. **75**, 1518 (1995).

[40] S. W. Morris, J. R. de Bruyn, and A. May, Phys. Rev. Lett. **65**, 2378 (1990).

[41] S. W. Morris, J. R. de Bruyn, and A. May, Phys. Rev. A **44**, 8146 (1991).

[42] M. Kléman, Rep. Progr. Phys. **52**, 1455 (1989).

[43] P. C. Martin, O. Parodi, and P. Pershan, Phys. Rev. A **6**, 2401 (1972).

[44] A. Saupe, Mol. Cryst. Liq. Cryst. **7**, 59 (1969).

[45] H. Pleiner and H.R. Brand, in *Pattern Formation in Liquid Crystals*, edited by A. Buka and L. Kramer (Springer, Berlin, 1996) p. 15.

[46] H. Pleiner and H. R. Brand, to be published

[47] S. Ried, Elektrisch getriebene Konvektion in smektischen Filmen, PhD Thesis, University of Essen, (unpublished), 1997.

[48] S. Ried, H. Pleiner, W. Zimmermann, and H. R. Brand, Phys. Rev. E **53**, 6101 (1996).

[49] H. R. Brand and H. Pleiner, Phys. Rev. A **35**, 3122 (1987).

[50] L. Kramer *et al.*, Liquid Crystals **5**, 699 (1989).

[51] H.R. Brand and H. Pleiner, J. Phys. (Paris) **43**, 853 (1982).

[52] W. Zimmermann, in *Defects, Singularities and Patterns in Nematic Liquid Crystals, NATO Advanced Study Institute Series*, edited by J. Coron, F. Helen, and J. Ghidaglia (Kluwer, Dordrecht, NL, 1991).

[53] G. Iooss and D. D. Joseph, *Elementary Stability and Bifurcation Theory* (Springer, Berlin, 1980).

[54] D. Avsec and M. Luntz, Compt. Rend. Acad. Sci Paris **203**, 1140 (1936).

[55] A. J. Rich, J. L. Sproston, and G. Walker, in *Eighth International Conference on Conduction and Breakdown in Dielectric Liquids*, edited by G. Molinari and A. Vivani (IEEE, New York 1984) p. 366.

[56] M. Suzuki, Phys. Rev. A **31**, 2548 (1985).

[57] P. Atten and L. Eloudie, J. Electrostatics **34**, 279 (1995).

[58] F. Argoul and A. Kuhn, Physica A **213**, 209 (1995).

[59] R. Chicon, A. Castellanos, and E. Martin, J. Fluid Mech. **344**, 43 (1997).

[60] S. Faetti, L. Fronzoni, and P. Rolla, J. Chem. Phys. **79**, 1427 (1983).

[61] S. Faetti, L. Fronzoni, and P. Rolla, J. Chem. Phys. **79**, 5054 (1983).

[62] Z. A. Daya, S. W. Morris, and J. R. de Bruyn, Phys. Rev. E **55**, 2682 (1997).

[63] V. B. Deyirmenjian, Z. A. Daya, and S. W. Morris, Phys. Rev. E **56**, 1706 (1997).

[64] A. Becker, S. Ried, R. Stannarius, and H. Stegemeyer, Europhys. Lett. **39**, 257 (1997).

[65] C. Langer, R. Stannarius, A. Becker, and H. Stegemeyer, Proc. SPIE, **3318**, 154 (1998).

[66] C. Langer and R. Stannarius, Phys. Rev. E **58**, 650 (1998).

[67] Figure by courtesy of Christian Langer.

*) present address: Theoretische Physik, Universität Saarbrücken, D 66041 Saarbrücken